

Master's thesis

**Analysis of internal structure of propellants with  
X-ray microtomography**

Author:

**Lenni Syrjänen**

Instructors:

**Arttu Miettinen  
(Taneli Laamanen)**



**University of Jyväskylä**

Department of Physics

Physics

August 9, 2023

# Abstract

Syrjänen, Lenni

Inner structure analysis of gun powder with X-ray tomography

Master's thesis

Department of Physics, University of Jyväskylä, 2023, 64 pages.

Gunpowder is an ancient multipurpose invention from 9<sup>th</sup> century in China. The chemical composition and physical structure of gunpowder have been developed for centuries to fulfill many purposes which lead into the development of smokeless powder or propellants. Knowledge about the chemistry surrounding propellant is vastly studied and known but precise study of the interior structure of individual propellant grains are lacking. This study validates X-ray microtomography as a method to analyse the inner physical structures of propellant grains from 18 different batches. I measured two grains from each batch. My focus of interest was on interior material domain identification, their sizes, porosity, pore sizes and the correlation of these with the recipe of the propellant. To aid my analysis I used a Python script and batch specific recipes for almost all of the batches provided by Nammo Vihtavuori Oy. Particles identified from the images are nitrocellulose, potassium bitartrate, potassium sulfate, surface finishing compound and two metals: tin and bismuth. Identified components do not change their original grain like shape while inside propellant and their size is also preserved. However, variations inside the batches are high, resulting in different sized particles and pores in varying locations for each grain. Potassium nitrate salt had the only notable correlation to the inner structure of propellant grains: the more there was salt the higher the porosity and thinner the walls between the pores are. Unfortunately, large variations in the atomic number of component elements introduced artifacts into the images, and high variations between grains prevented me from gathering statistically relevant data. Nevertheless, imaging of propellant with X-ray tomography (X-CT) has proven useful giving lots of previously unknown information of the physical structure of propellant grains and their composition, which can be used to develop new improvements to propellant. Method could also be improved on to gain more precise information about the propellant, for example reducing the image artifacts.

Keywords: Gunpowder, Propellant, X-ray tomography, potassium bitartrate, potassium sulfate, potassium nitrate, tin, bismuth, nitroglycerin, nitrocellulose.

# Tiivistelmä

Syrjänen, Lenni

Inner structure analysis of gun powder with X-ray tomography

Pro gradu -tutkielma

Fysiikan laitos, Jyväskylän yliopisto, 2023, 64 sivua

Ruuti on muinainen monikäyttöinen keksintö jo yhdeksänneltä vuosisadalta Kiinasta. Sitä on historian aikana käytetty ja muokattu moneen tarkoitukseen, niin kemiallisesti kuin fyysikaalisesti ruutijyvän geometriaa muuttamalla. Ruudin kemiallinen rakenne on tarkasti tiedossa ja sen kemiallisia ominaisuuksia on tutkittu laajasti, mutta sisäistä rakennetta ei ole tutkittu tarkasti, ainakaan julkisesti. Tässä työssä olen kuvantanut yksittäisten ruutijyvien sisäistä rakennetta 18 eri ruutierästä röntgenmikrotomografiaa hyväksi käyttäen ja arvioinut, kuinka hyvin menetelmä sopii ruudin analysointiin. Keskityin erityisesti ruudin sisältä löytyneiden partikkelien tunnistamiseen, ruutijyvien huokoisuuteen ja huokosten kokoon, sekä siihen kuinka ruudin valmistuksessa käytetyt komponentit ovat vaikuttaneet sisäiseen rakenteeseen. Käytin analyysin apuna ohjaajani A. Miettinen pohjustamaa Python ohjelmaa, sekä ruutien ainesosataulukkoja Nammo Vihatavuori Oy:ltä (taulukkoja ei ole esitelty työssä). Kuvista pystyin tunnistamaan selkeästi eri tiheisiä materiaaleja, kuten nitroselluloosaa, viinikiveä, kaliumsulfaattia, pintakäsittelyaineita ja kahta metallia: tinaa ja vismuttia. Havaitsin myös, että tunnistetut komponentit eivät muuta muotoaan valmistuksen aikana, vaan pitävät alkuperäisen raemaisen muotonsa ja kokonsa lopullisessa ruudissa. Komponenttien koko ja sijainti vaihtelivat ruutijyvissä suuresti ruutierien sisällä, tein saman huomion myös ruudin sisäisille huokosille. Kaliumnitraatti-suola oli ainut ruudin komponenteista, jolla oli selkeää vaikutusta sisäiseen rakenteeseen: Suolan määrän lisääntyessä ruutijyvän huokoisuus kasvaa ja seinämien paksuus huokosten välillä kapenee. Kuvissa on kuitenkin paljon artefakteja ja ruutijyvien keskinäisen rakennevaihtelun takia tilastollisesti merkittävää dataa ei voitu kerätä. Siitä huolimatta ruutijyvien kuvantaminen on osoittautunut hyödylliseksi, antaen paljon tietoa ruudin sisäisestä rakenteesta, jota voidaan käyttää tulevaisuudessa uusien ruutien kehittämiseen. Menetelmä on ruudille uusi, joten jos esimerkiksi artefakteja voitaisiin vähentää tulokset voisivat olla tarkempia ja kuvista saataisi vielä enemmän informaatiota ruudin sisäisestä rakenteesta.

Avainsanat: Ruuti, Röntgentomografia, huokoisuus, viinikivi, kaliumsulfaatti, kaliumnitraatti, tina, vismutti, nitroglyseriini, nitroselluloosa.

## Prologue

This study was proposed to me by Taneli Laamanen from Nammo Vihtavuori Oy and I would like to thank him, Nammo and my instructor from university Arttu Miettinen for their support and trust on my skills. I was provided with excellent information from both ends and given all the required training and equipment to make this project/study. Project was originally internship at Nammo but we decided that it would make a good subject for Master's thesis. Lastly I would also like to thank Meeri Nimell and Joni Parkkonen who instructed me when Miettinen and/or Laamanen were not available.

August 9, 2023

Lenni Syrjänen

# Contents

<b>Abstract</b>	<b>I</b>
<b>Tiivistelmä</b>	<b>II</b>
<b>Prologue</b>	<b>III</b>
<b>1 Introduction</b>	<b>1</b>
<b>2 Materials and methods</b>	<b>2</b>
2.1 Gunpowder and propellants . . . . .	2
2.1.1 Grain geometry . . . . .	2
2.1.2 Nitrocellulose . . . . .	3
2.1.3 Black gunpowder . . . . .	4
2.1.4 One-component propellant . . . . .	5
2.1.5 High energy one-component and two-component propellant .	6
2.1.6 Other propellant types . . . . .	8
2.1.7 Studied propellants and relevant components . . . . .	8
2.2 X-ray tomography . . . . .	9
2.2.1 Introduction . . . . .	9
2.2.2 X-ray production . . . . .	9
2.2.3 X-ray attenuation . . . . .	11
2.2.4 X-ray detectors for imaging . . . . .	13
2.2.5 X-ray imaging . . . . .	14
2.2.6 X-CT setups . . . . .	15
2.2.7 Reconstruction . . . . .	18
2.2.8 Artifacts . . . . .	22
2.3 Measurements and image analysis . . . . .	27
2.3.1 Device used . . . . .	27
2.3.2 Sample preparation . . . . .	27
2.3.3 Image analysis . . . . .	29
<b>3 Results</b>	<b>36</b>
3.1 Material phases visible in the images . . . . .	36
3.2 Quality of images . . . . .	40
3.3 Image analysis with Python script . . . . .	42
<b>4 Discussion</b>	<b>46</b>
<b>A Python script for image analysis in this thesis</b>	<b>59</b>

# 1 Introduction

Gunpowder is an ancient invention, first found by the Chinese in the 9<sup>th</sup> century [1, 2] but the recipe was published by Roger Bacon later, in 1248. Originally, gunpowder was used in fireworks, but quickly after the recipe became common knowledge, people started using it in guns and explosives [3]. This gunpowder was so called black gunpowder, which was later replaced with nitrocellulose (NC) based smokeless powder or propellant, after the founding of sulfuric acid and its possibility to energise cellulose in the 1840s [2–4]. Black gunpowder was always spherical, but newly found NC could be molded into desired shapes, affecting the burning properties of the propellant [4]. This kind of propellant is called one-component propellant. Alfred Nobel invented the gelatination of NC propellant with nitroglycerin, leading to the development of higher energy two-component propellant [4]. Currently, propellant and gunpowder are used, for example, in fireworks, gun ammunition, small and medium-sized rockets, and explosives, making them very versatile tools in many fields. The chemical composition of propellants is well known and studied, and their physical structure is regulated in some degree to attain the desired structure and burning properties. However, no detailed (public) studies have been made about the interior of single propellant grains. Some have studied the bulk of propellant, for example, with neutron tomography [5], but I will study the inner structure of propellant with X-ray microtomography (X-CT).

As the name implies, X-ray tomography uses X-rays with computer calculations to form 3D images of the interiors of a solid object of interest. Found in 1895 by Wilhelm Conrad Röntgen, X-rays were first used to take projections of solid objects, with the medical field heavily investing in them early on [6]. The non-invasive nature of X-ray images allowed physicians to locate foreign bodies before surgery, reducing the surgery time [6]. After the computer revolution, the first X-CT device was developed by Sir Godfrey Hounsfield in 1967 and was quickly deployed in the medical field [7, 8]. This Nobel Prize-winning innovation was used for the first time on humans in 1971, and in 1973, CT scanners were used clinically [9]. These days, wood technology, paleontology, soil, marine and geo-sciences utilize X-CT along with medical and material sciences [10–15]. Development on the X-CT devices finally led to micro-X-CT capable of sub-micrometer resolution.

In this study, I used micro-X-CT to measure one- and two-component propellant grains individually to evaluate how well the method is suited for propellant analysis. I also used a Python script to further analyze the images quantitatively. My focus was on particle identification, pores and how the inner structure is affected by the propellant components in different batches. This kind of study has never been done with propellants before, but X-CT has been used and found beneficial in studies of other similarly porous samples [16–18].

## 2 Materials and methods

### 2.1 Gunpowder and propellants

Gunpowder, or black gunpowder, is an old invention and has been used widely throughout history. These days, it is used, for example, in guns, cannons, small and medium-sized rockets, explosive weaponry, airbags and fireworks. [1, 2] These days, propellants are more common than gunpowder. The basic function of propellant is still the same as gunpowder's, as it transfers chemical energy into a change in volume [2]. Explosion of propellant is a fast exothermic oxidation reaction that releases gases [2]. However, depending on the variety and type of propellant, the conditions for initiating detonation and explosion quality may vary (pressure and temperature). For example, varieties studied in this thesis are optimized to detonate at over two times the atmospheric pressure, meaning that the detonation at the chamber of a X-CT device is highly unlikely. In this section, I will go over simple geometries for propellant grains, different propellant types, how they are used, manufactured, and modified for their purposes, and varieties of propellant studied in this study. Also, I will briefly touch on the chemical components of the materials and some other propellant types, to give some perspective on the subject. The names and batch numbers of the studied propellant batches and some components are naturally replaced with code names to protect company information. Finally, I will go over relevant variety specific information about the studied powders. First, I will introduce how grain geometry affects burning.

#### 2.1.1 Grain geometry

There are four main geometries for propellant grains: sphere, flake, tubular and panel [2, 19]. Tubular grains are cylinders with a hole or multiple holes going through them. All main geometries are introduced in figure 1. Geometry effects the burning properties of propellants [20]. Burning area of a grain can increase (progressive propellant), decrease (degressive propellant) or stay the same (neutral propellant) while burning, depending on the shape of the grain. The inner structure of the grain affects the progression of burning. Multi-holed tubes have only progressive geometry, sphere, panel and cylinder are degressive, and flake and single-holed tubes are neutral. However, these can be changed if the grain has pores inside; grains with high porosity are often progressive. Progressive propellants rise pressure more steadily, while degressive propellants rise pressure fast but also lower it quickly. Neutral propellant is an intermediate between the other two. [2]

In addition to their geometry, propellants can be separated based on their use (e.g., cannon, rifle and fireworks), chemical structure (homogeneous or heterogeneous)

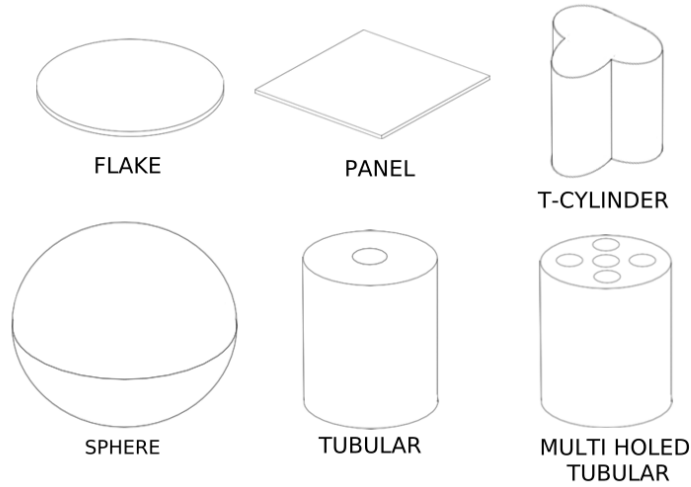
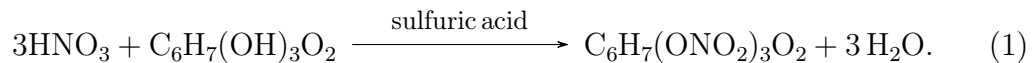


Figure 1: *Basic propellant grain geometries and a less common geometry in which the cross-section has the shape of the letter T, called here the T-cylinder.*

or chemical composition. The latest one is the most common and is also used here. The propellant types discussed here are black gunpowder, one-component, two-component, multi-component and composite propellant. I will start by going over the main component of the studied propellant types, nitrocellulose, and then continue with different types of propellant.

### 2.1.2 Nitrocellulose

Nitrocellulose (NC) is main component in one- and two-component propellants. NC is a result of the nitration of cotton or wood cellulose [2, 20]. Cellulose consists of chains of glucose molecules, whose chemical formula is seen in figure 2a. Each of the glucose molecules can be nitrated up to three times. Hydrogen group(s) of cellulose (HO) is/are replaced with nitro group(s) (NO<sub>2</sub>) using strong nitric acid (HNO<sub>3</sub>) [21]. Depending on the level of nitration, the nitrogen concentration is in order from nitration levels 1 to 3: 6.76 %, 11.11 % and 14.15 %, but in practice, 13.5 % is the maximum limit [2, 22]. A practical limit can be achieved Schöben method, in which a mixture of sulfuric and nitric acids is used, contrary to only nitric acid [23]. The reaction of the Schöben method is as follows:



One- and two-component propellant properties are effected by the nitration level of the NC, which can be easily controlled [23].



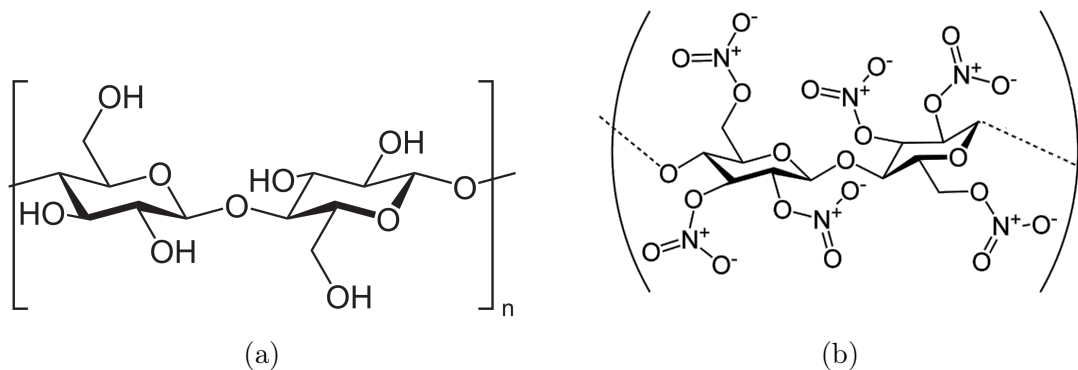


Figure 2: Chemical structure of a) cellulose and b) nitrocellulose (NC). Nitration level of the NC is 3 in the image b).

NC is unstable and goes through degradation. The degradation reaction is exothermic and self-catalyzing, started by the breaking of  $-\text{O}-\text{NO}_2$  bond and the release of  $\text{NO}_2$  [2, 24].  $\text{NO}_2$  rapidly complexes to nitrate group ( $\text{CONO}_2$ ) which is involved in a reaction to produce oxidation products [25]. NC is preserved in water, which promotes the hydrolysis reaction of the  $-\text{O}-\text{NO}_2$  bonds to produce  $\text{HNO}_3$  which catalyzes the release of more  $\text{NO}_2$ . Cyclical self-catalysis and self-heating lead to an uncontrollable situation.[26–28] Therefore, stabilizers (e.g., diphenylamine) are needed. Stabilizer reacts with  $\text{NO}_2$  preventing auto-catalysis. They do not react with other components and do not disappear in any other way than the desired reaction (e.g., no spontaneous evaporation).

Dry over 12.6 % NC is considered explosive [2]. The cotton-like structure makes it extremely easy to detonate with heat and knocking. NC is therefore stored and transported in a water or ethanol solution.

### 2.1.3 Black gunpowder

Like previously mentioned, black gunpowder was the first type to be discovered and the most simple, being only a mechanical mixture of  $\sim 75\%$  potassium nitrate ( $\text{KNO}_3$ ),  $\sim 10\%$  of sulfur (S) and  $\sim 15\%$  charcoal (C). Mixing must be done carefully because there is a risk of detonation when ingredients are mixed at such small particle sizes [4]. Black powder has a low specific energy, and due to its being a mechanical mix (heterogeneous), it releases black gas particles while burning, hence the name black gunpowder. Because it absorbs water from the environment effectively (has a high hygroscopy), it must be stored in a dry places. If stored in wet environments, it will absorb water, become unusable and be unable to detonate. All the powders are spherical and the only way to change the properties

of burning, and hence explosion, is to change the grain size; the bigger the grain, the slower it burns. These days, black gunpowder is outclassed as a propellant in many applications; however, due to its ability to burn well at room temperatures and pressures, it is still the best or cheapest option for some applications. The most common uses are fireworks, primer, and traditional shooting. [2]

#### 2.1.4 One-component propellant

One-component propellant, also called N-type, has one active component, NC, hence the name [2]. Process of making a single batch of N-type starts with mixing NC in mixture of ether and ethanol. At the same time, some components, like potassium nitrate ( $\text{KNO}_3$ ), tin (Ti), bismuth (Bi) and potassium sulfate ( $\text{K}_2\text{SO}_4$ ), are inserted into the mixture depending on the final propellant variety produced. The process is called gelatination. Gelatination time also varies depending on the final product. After gelatination, NC mass has a texture similar to clay, which can then be injected through a matrix (a mold, typically a metal plate with many small holes) into the desired shape, resulting in bundles. Bundles are dried so that the mixture content is 20-30 % and then cut into desired lengths. Here Nammo Vihtavuori uses a vacuum dryer to dry grains from excess ether-ethanol mixture; alternative options for removal would be heat, air current, or water. The product is now called "green powder". From here, the production process branches into two categories: one-component propellant types and high energy one-component propellant types. The full manufacturing process is introduced in figure (3). High-energy types will be considered later with two-component propellants due to their similar chemical composition. [29]

Considering it is a one-component propellant, green powder is coated with graphite and combustion regulating compounds. Coating allows transportation with lower combustion and detonation risks. Next in the process is water treatment, which removes all the remaining excess solvents from the propellant. Some coating can be done at the same time. Water treatment also mixes the batch, making it more homogeneous, which is important to ensure the quality of the batch. After drying the propellant batch to its equilibrium humidity at room temperature, the batch is mixed with another batch(es). Final mixing and screening are done to ensure the quality of the final product before it is packaged and stored or transported. [29]

N-type can be easily modified to fulfill different roles, from rifles to cannons, due to wet NC's clay like properties [2]. Propellant grain can have multiple different sizes and shapes, and even the inner structure can be adjusted. Examples of these can be seen in figure 1. The NC mass used to make N-types is homogeneous, resulting in smooth batches. However, it is notable that the quality of the end

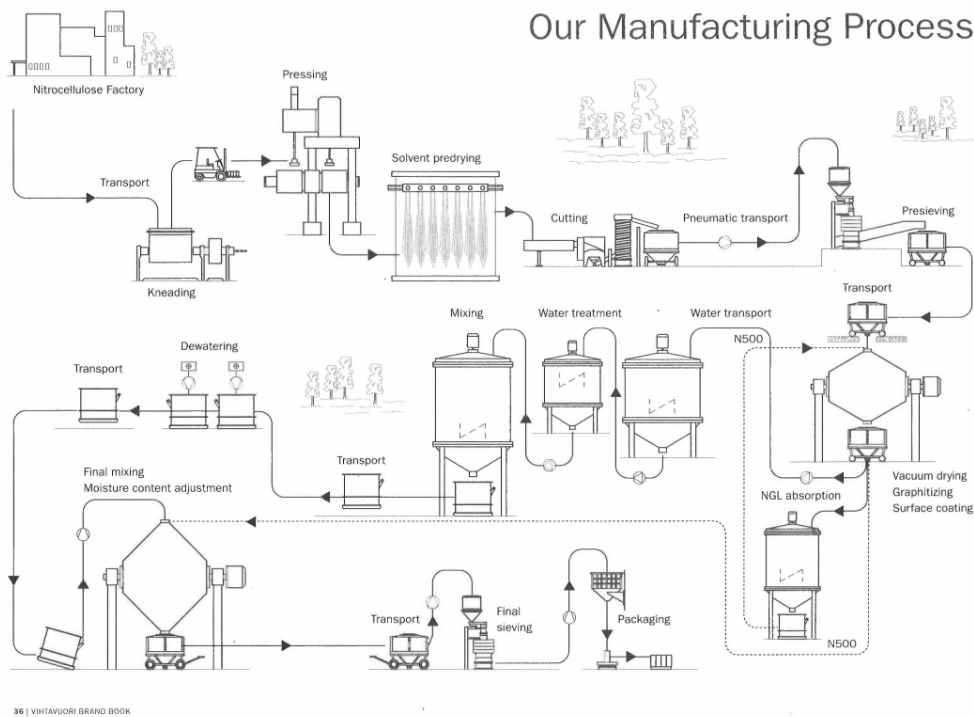


Figure 3: Chart of the production process used in Nammo Vihtavuori for one-component and high energy one-component propellants.

product is heavily affected by the quality of the NC. The specific energy to heat ratio of combustion is favorable in N-types, and they are also cheap to make [2].

As previously mentioned, dependence on NC quality is not the only weakness of N-types. Easily modified specific energy of the N-types can vary from 3000 J/g to 4100 J/g, which is better than black gunpowder has but is still too low for some purposes, like sniper rifles and ammo with heavy bullets [2]. Combustion is not optimized at normal pressures and therefore limits its use. Removal of solvent can take a lot of time with bigger cannon propellant varieties, slowing production. Similar to black gunpowder, N-types also absorb water from the environment effectively, requiring dry storage. However, the ability to absorb moisture can be reduced with additives.

### 2.1.5 High energy one-component and two-component propellant

Two-component and high energy one-component (HE-type) propellant types have two active components, NC and nitroglycerin (NGL) [2]. These two types are

similar from a chemical composition perspective, but the properties of the HE-type are closer to those of the N-type than those of a two-component propellant. The main difference between HE and two-component propellants is how NGL is added. In two-component propellants, the NGL is added during gelatination, and in HE-type propellants, the NGL is added to the green powder in the middle of the manufacturing process. I will start with the production of HE-type and then continue to two-component.

Like previously mentioned, the manufacturing of HE-type is identical to that of N-type until green powder has been produced. Green powder is inserted into a reactor with a NGL ethanol solution. Stabilizers are added at the same time. NGL content of 25 % can be reached with this method. In the same reactor, grains are surface finished with undisclosed organic polymer, which will be known later as SFC. NGL and surface finishing compound absorption are boosted with surface-active compounds. Unfinished propellant is mixed for multiple hours inside the reactor before the ethanol is drained with a vacuum dryer. The final product is left with some concentration gradient of NGL and other compounds inserted in the reactor; in other words, there are more compounds on the perimeter of the propellant grain than inside. Then propellant is washed with warm water, dried to its hygroscopic equilibrium, screened, mixed and packaged. [29]

Due to NGL, HE-type has higher specific energy than N-type, which enables its use in sniper rifles, heavy bullet ammunition, and rifles with heavy bullets that require high muzzle velocity (N-type can not be used here). Other uses are grenade launcher ammunition, middle caliber ammunition, and some shotgun ammunition. Like N-type, HE-type can also be easily modified due to the main ingredient being NC; in addition, NGL content can be modified to further regulate the burning properties. However, HE-type specific energy is still too low for some uses. There, a two-component propellant is used, which has a higher NGL content. [2]

For two-component propellants, insertion of NGL happens at gelatination. It requires 40-50 % NGL to NC mass mixture. In addition, there are water and other compounds present while the mixture is mixed. Two-component propellants can have NGL content up to 50 % in which point NGL starts to affect the plasticity of the mass [2]. Water is removed first with a centrifuge and then by waltzing the mass between two heated rolls. The end result is a warm mass that can be pressed into desired shapes, like previously with N and HE types. Grains are then packaged and stored. NGL content gives a high specific energy of 3300 – 5200 J/g [2]. Therefore, two-component propellant suits higher-energy purposes like grenades, special rifles, and small and medium-sized rockets. It is also faster to manufacture because there are no solvents that need to be removed, like with N-type.

For both HE-type and two-component propellants, the main weaknesses originate in the use of NGL. NGL is a toxic substance; it evaporates and combusts easily. It also increases the heat released from burning, which can overheat the weapon and strain the barrel of the gun. NGL can also migrate into ammunition cases, which can be dangerous and limit its use due to safety considerations. Two-component propellant is also less plastic due to its higher level of NGL, limiting the possible geometries a little. [2, 29]

### 2.1.6 Other propellant types

Other types of propellant are multi-component and composite propellants. Multi-component propellants have, in addition to NC and NGL, other energetic components that enhance ballistic properties or lower the temperature of the burning. Multi-component propellants can be made with a two-component propellant process. Due to its high energy content, multi-component propellant is mostly used in artillery and tank ammunition. [2]

Composite propellant is not NC-based but uses inorganic salt as an oxidizer, most commonly ammonium perchlorate ( $\text{NH}_4\text{ClO}_4$ ). The composition is nonhomogeneous and consists of inorganic salts, polymers and additives. The properties of composite propellant make it easy to modify and large uniform bulks can be made from it, making it useful as rocket fuel. The detonation temperature can also be modified to be high, making it a low-risk propellant to transfer and store. [2, 3]

### 2.1.7 Studied propellants and relevant components

In this study, I used N-type, HE-type, and two-component propellants. I had 18 different batches, of which some were made for the same purpose (same variety), some had similar properties, and others were totally different. Grains from all batches had one hole going through them, but grains from three batches had none. All batches also had small grain sizes, with diameter varying from about 0.6 mm to 1.1 mm and height at about 1.0 mm to 1.5 mm (variation is high). I had 8 batches of N- and HE-types and 2 batches of two-component propellant. Batches are named N1-N8 (N-types), H1-H8 (HE-types) and T1 and T2 (two-component). Although I had access to recipes for N and HE -type batches I will not go in detail about the chemical composition of each batch, as that might disclose confidential information and is not necessary in this thesis. I will only mention if relevant components should or should not be found inside the batch.

Relative compounds for this study are NC ( $\text{C}_6\text{H}_9(\text{NO}_2)_m\text{O}_5$ , where m is {1,2,3} indicating level of nitration), NGL ( $\text{C}_3\text{H}_5\text{N}_3\text{O}_9$ ), potassium nitrate ( $\text{KNO}_2$ ), potassium sulfate ( $\text{K}_2\text{SO}_4$ ), potassium bitartrate ( $\text{KC}_4\text{H}_5\text{O}_6$ ), tin (Sn) and bismuth (Bi).

All of the compounds are included in some of the grains. One surface finishing compound is also relevant and it will be called SFC in the future but will not be named due to confidentiality reasons. Like mentioned before in sections 2.1.4, and 2.1.5 N-type propellants do not have NGL in them, but HE-type and two-component propellants do. However, batch H2 was specifically made for my studies without NGL; otherwise, it is identical to batch H1. Also, it is notable that  $K_2SO_4$  is only found in batches of HE-types and SFC is on top of HE-types.

## 2.2 X-ray tomography

### 2.2.1 Introduction

Since the discovery of X-rays by Wilhelm Röntgen in 1896, X-rays have been used to take non-invasive X-ray images, which are projections of a solid 3D sample. This is a widely used application in the medical field as well as industry and research [6]. In 1970s, X-ray computer tomography, or X-CT, was developed, utilizing multiple X-ray images taken from different perspectives of the sample [7]. A specific algorithm is used to reconstruct them into a 3D image. CT allows 3D imaging of solid samples with good resolution. It uses X-radiation with wavelengths from 10 nm to 0.01 nm. Wavelengths correspond to energies from about 0.124 keV to 0.124 MeV. Energies are high enough to penetrate solid objects and can ionize molecules and atoms. In this section, I will go over the principles and weaknesses of X-ray imaging and X-ray tomography. The algorithm used to reconstruct the images is introduced later. Finally, I will go over sample selection and preparation.

### 2.2.2 X-ray production

The most common way to produce X-rays is with an X-ray tube (X-tube). Electrons are accelerated with some voltage over 0.124 kV and focused on a metal anode, where electrons collide with the metal surface. [30] An anode is also called a target. There are two processes in which the X-rays are produced: bremsstrahlung, or breaking radiation, and characteristic X-rays [31]. Breaking radiation comes from the electrons interacting with the electric field of the nucleus of the target. This scatters electrons and therefore decelerates them quickly, releasing photons as X-rays or  $\gamma$ -rays, if kinetic energy of the electrons is high enough. The radiation spectrum is continuous, with the maximum being at electron charge times acceleration voltage, where all the kinetic energy of the electron is released as an X-ray photon.

Characteristic X-rays depend on the target metal. Accelerated electrons have high kinetic energy, which can knock the inner electrons of the target out of their orbitals. An electron from a higher energy orbital will fill the spot, releasing

a photon with energy equal to the energy difference between the two orbitals. The energy difference is in the range of X-rays. An electron can be knocked from multiple different orbitals, like K and L, and a filling electron can come from multiple different orbitals, like 2p or 3p. X-rays can therefore have multiple different energies. Energies can only be equal to the difference between the orbital energy of the knocked-out electron, and the orbital energy of the filling electron. Electrons with a higher binding energy than the kinetic energy of the accelerated electron can not be knocked out of the orbital, limiting the maximum energy of the characteristic X-rays. The X-ray energy spectrum has spikes characteristic of the target.

The total X-ray spectrum produced by an X-ray tube is combination from Bremsstrahlung and characteristic radiation. In my measurements, I used 60 kV acceleration voltage and tungsten as target materials, yielding the spectrum in figure 4.

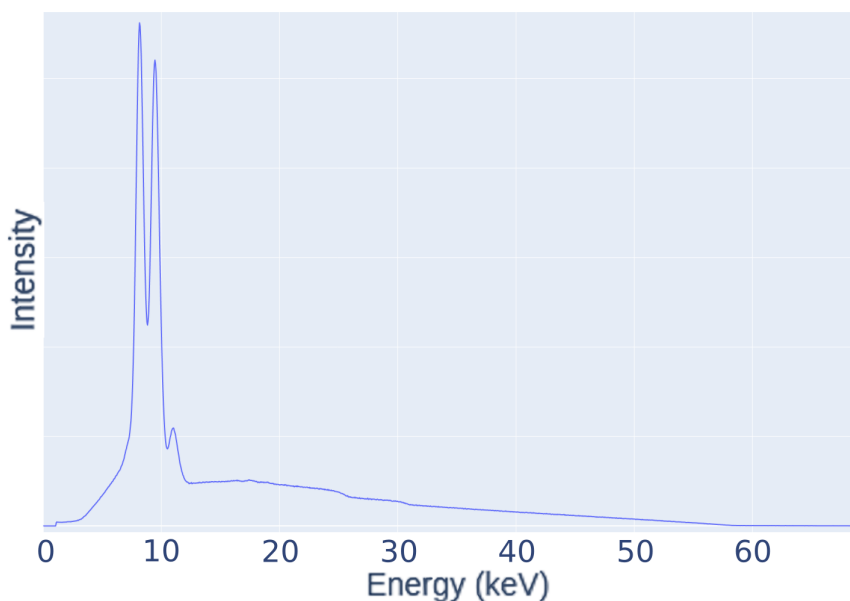


Figure 4: *X-ray spectrum from Xradia  $\mu$ X-CT device located at University of Jyväskylä. Source has a tungsten target and acceleration voltage is 60 kV.*

Another possible X-ray source is a synchrotron [32]. Synchrotron sets electrons on a circulating path. X-rays are emitted similarly to bremsstrahlung; electrons are accelerated by forcing them on a circular path. The acceleration is produced by bending magnets or insertion devices, such as undulators or wigglers, which force the electrons to move on a sinusoidal path. Produced radiation has orders of magnitude higher flux than X-ray tubes and a monochromatic beam is often

selected for the measurements. Monochromatic beam improves sensitivity to small differences in absorption and limit artifacts [32, 33].

The X-ray tube is cheaper and therefore more common, but due to its lesser flux of radiation and polychromatic energy spectrum, synchrotrons are used in advanced research facilities [32]. Reasons for this will become clear in the following when I discuss X-ray attenuation in material and artifacts seen in X-ray tomography images.

### 2.2.3 X-ray attenuation

Attenuation of X-rays originates from interactions between X-rays and electrons of atoms in the sample: photoelectric effect, Compton scattering and Rayleigh scattering. Each of the interactions impact on the attenuation coefficient  $\mu$ , which is a material-specific constant used to determine how much X-rays are attenuated in that material [34]. There are two ways to express attenuation coefficient: Linear attenuation coefficient, which is related to the distance the radiation travels inside the material, and mass attenuation coefficient  $\mu_m$ , which is related to mass thickness, i.e., amount of mass on the path of the X-ray [34].

Attenuation coefficient  $\mu$  can be written as the sum of attenuation originating from photoelectric effect  $\mu_e$ , Compton scattering  $\mu_c$  and Rayleigh scattering  $\mu_r$  [34]:

$$\mu = \mu_e + \mu_c + \mu_r. \quad (2)$$

Similarly, for the mass attenuation coefficient  $\mu_m = \mu_{me}\rho + \mu_{mc}\rho + \mu_{mr}\rho$ , in which  $\mu_{me}$ ,  $\mu_{mc}$  and  $\mu_{mr}$  are mass attenuation coefficients for the photoelectric effect, Compton scattering and Rayleigh scattering, respectively. All of these are dependent on the material and atoms the X-rays are interacting with.

The attenuation coefficient does not depend alone on the species of penetrated material but also on the energy of the X-rays  $E$ . Higher-energy X-rays penetrate materials better, giving them a lower attenuation coefficient. If the sample is not homogeneous, the attenuation coefficient varies depending on the location inside of the sample, giving it a relation to the position inside the sample. The linear attenuation coefficient is therefore  $\mu(s, E)$  for polychromatic X-rays, which is also true for the different sources of the attenuation in equation (2) [34, 35]:

$$\mu(s, E) = \mu_e(s, E) + \mu_c(s, E) + \mu_r(s, E). \quad (3)$$

This also means that the intensity of X-ray beam passed through the sample (penetration intensity) has an energy dependence  $I(E)$ .



The atomic number  $Z$  of the penetrated materials affects the attenuation coefficient  $\mu$  as  $\mu_e$  has a clear relation to atomic number, such as [34]

$$\mu_e = \alpha \rho \frac{Z^k}{E^l}. \quad (4)$$

All of the variables  $\alpha$ ,  $k$  and  $l$  are constants, where classically  $k = 3$  and  $l = 3$  [34]. For numerical fits into experimental data,  $k \in [3, 4]$  and  $l \in [3, 3.5]$ . The equation (4) demonstrates an important relation between the atomic number and attenuation, which can be used to identify materials using X-rays and explains why denser materials with elements with a higher atomic number attenuate X-rays strongly [30, 32, 34, 36].

In this section, I will start with homogeneous linear attenuation and then expand into heterogeneous and energy-dependent cases. Later, I will return to X-ray attenuation theory in the section about reconstruction and expand the theory into practical use.

If radiation is monochromatic with an initial intensity  $I_0$  it will fulfill Beer's law:

$$I = I_0 e^{-\int^d \mu(s) ds}, \quad (5)$$

where  $I$  is the intensity after the X-ray passed through the sample,  $\mu(s)$  is (linear) attenuation coefficient of the material as a function of the distance  $s$  traveled inside the material and  $d$  is the total thickness of the material. Variables are illustrated in figure 5. Note that in practice, the initial intensity  $I_0$  is the intensity measured without a sample between source and detector.

Beer's law can also be written using the mass attenuation coefficient  $\mu_m(s) = (\mu/\rho)(s)$  and mass thickness  $x = \rho d$  as [32]

$$I = I_0 e^{-\int^x \mu_m \rho ds}. \quad (6)$$

In both equation (5) and (6) the path is considered to be a line and will be a line in the equations below. Note that if the sample is homogeneous, equations (5) and (6) give

$$I = I_0 e^{-\mu d} \quad (7) \quad I = I_0 e^{-\mu_m x}. \quad (8)$$

respectively. Equation (7) demonstrates how X-radiation is attenuated more the longer the path is, or in practice, the thickness of the sample.

Usually, the sample is not homogeneous but consists of materials with different attenuation coefficients on different parts of the path, each attenuation coefficient

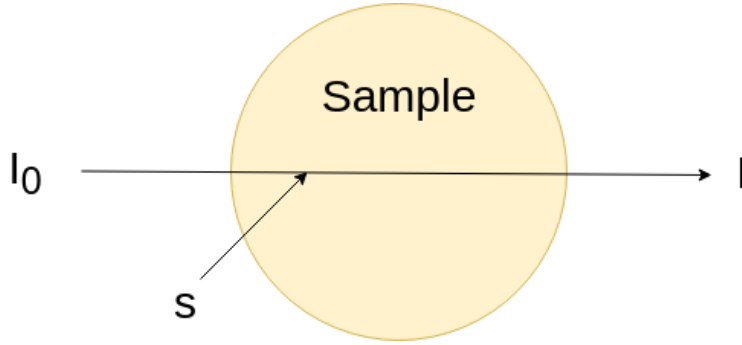


Figure 5: Illustration of X-ray penetrating a sample and attenuating from initial intensity  $I_0$  into  $I$  along a path consisting of points  $s$ .

$\mu_i$  is then valid for a distance  $d_i$  of the total distance  $d$ , converting equations (5) and (6) into

$$I = I_0 e^{-\sum_i \int^{d_i} \mu_i(s) ds} = I_0 e^{-\sum_i \mu_i d_i} \quad (9)$$

$$I = I_0 e^{-\sum_i \int^{x_i} \mu_{mi}(s) ds} = I_0 e^{-\sum_i \mu_{mi} x_i} = I_0 e^{-\sum_i \frac{\mu_i}{\rho_i} x_i} \quad (10)$$

Here  $x_i = d_i \rho_i$ , where  $\rho_i$  is the density of material corresponding to the attenuation coefficient.

I previously mentioned how attenuation coefficient has a relation to X-radiation energy and how high-energy X-rays penetrate material better than lower-energy ones. This, along with equation (9), means that if the energy of the X-rays is too low, almost all of it attenuates and the detected signal is too low for measurements and if the energy is too high, almost all X-rays penetrate the sample, giving a bad contrast and resolution [37]. Balancing between the proper strength of the signal and resolution is one of the challenges of X-ray imaging and X-CT [32]. Optimal resolution is acquired when the attenuation coefficient  $\mu$  is  $2/d$ , corresponding to about 14 % of X-radiation penetration [37]. Note that this number is calculated with strong assumptions that might not be realistic in all practical cases.

#### 2.2.4 X-ray detectors for imaging

In X-ray imaging and X-CT, the most common type of detectors are area detectors, which measure the intensity of the penetrating X-radiation coming into each pixel. The first this kind of detector was a photographic film, typically consisting of silver bromide (AgBr), where AgBr is in crystal form. When exposed to X-radiation, it ionizes, and free electrons are trapped inside crystal defects. Silver atoms are attracted by the defects and reduced. This forms clusters of transparent silver atoms, which are converted to opaque silver atoms in the developing process. The

image is darker in the areas that received more radiation. Unfortunately, the use of film detectors in X-CT scanners would be difficult because each projection taken need to be digitalized for the computer to be able to reconstruct a 3D image. However, it is possible but becomes harder the more projections are needed. [38]

More modern methods usually convert X-rays into visible light and then into electric signals, achieved via a scintillator. A scintillator is composed of a fluorescent material that X-rays can excite [39, 40]. The excited state is then released and photons in the visible light spectrum are released. There are 19 commonly available inorganic scintillator crystals and only three organic ones [40, 41]. Higher density and atomic number materials are used in scintillators for higher energy applications and lower density and atomic number materials are used for low energy applications [32, 40]. In detectors visible light from scintillators is transformed into an electrical signal via an array of complementary metal-oxide semiconductors [32]. This is basically a digital camera.

### 2.2.5 X-ray imaging

Like previously mentioned, an X-ray image is a projection of a solid 3D object. Images are usually gray images (they can be color coded), where each pixel has a value representing the ratio of X-ray intensity with out the sample between source and detector  $I_0$  and the intensity of X-rays which penetrate the sample  $I$  as

$$\frac{I}{I_0} = e^{-\sum_i \frac{\mu_i}{\rho_i} x_i}. \quad (11)$$

This can be impressed as a logarithmic relation:

$$\ln\left(\frac{I_0}{I}\right) = \sum_i \frac{\mu_i}{\rho_i} x_i = \sum_i \mu_i d_i \quad (12)$$

which is more used when solving attenuation coefficient  $\mu$  [42]. Comparing  $I_0$  and  $I$  is important due to the fact that X-ray sources do not give uniform X-radiation into each detector pixel and if only  $I$  was measured the resulting projection would not not represent the sample. This is even more important when considering X-CT imaging. The method of using images without samples to correct images is called flat field correction. [32].

According to equation (12) the X-ray images (not X-ray tomography images) differentiate pixels depending on the total attenuation through each path, depending on the attenuation coefficient along those paths and the lengths of the paths. The image consists of pixels, and each pixel corresponds to a single line path through the sample. However, if two paths have the same total attenuation through the

sample, it will lead to the same pixel value among the two pixels. This does not mean that the paths are identical. One possible situation is introduced in figure 6(a), where there are four paths and each has the same pixel value.

In the figure 6(a) paths 1 and 2 are identical, as are 3 and 4, but 1 and 3 are not and therefore 1 and 4, 2 and 3, and 2 and 4 are different. Due to X-ray images only giving projections of the sample, it can not identify the order in which the components are on a given path. From the resulting X-ray image in figure 6(a) one could say that all four paths are identical but also that all the paths are different. To improve the spatial knowledge of the sample, one must take another image from a different perspective, as seen in figure 6(b). The total volume of the sample can now be divided into pixels (figure 6(c)). It can be concluded that inside the sample there are one to two particles on columns 2 and 4 in a way that each row has one or part of one such particle. This particle is marked in the images with an attenuation coefficient  $\mu_3$ . Two other materials can not be detected with the two images taken and would require more perspectives, which would also enable pinpointing the exact location of particles with  $\mu_3$ . In the case of more complex samples, more perspectives are required. This also requires more complex methods of compiling the images into 3D images of the inner structures of the sample, meaning proper algorithms and computer calculations.

### 2.2.6 X-CT setups

In the end of the last section, I described the analysis of a simple sample with two X-ray images from two perspectives  $90^\circ$  apart. An example can be thought of as X-CT in its simplest form. However, X-CT uses hundreds to thousands of X-ray images from different perspectives to form a 3D image of the interiors of the sample [32, 43]. Separate 3D images can also be taken at time intervals, making them 4D images representing changes through time in the interior of the sample [32]. Images do not consist of area elements, or pixels, but instead of a volumetric substitute for a pixel, a voxel. A voxel is the smallest cubic volume element in a 3D image. A typical measurement device consists of an X-ray source and detector and a sample stand. The exact configuration depends on the device.

The X-ray source and detector can be either moving or stationary during measurements, basic setups are presented in figure 7. In moving configuration presented in figure 7(a), the sample is stationary and needed perspectives are acquired by moving the source-detector pair. This is essential if the studied structures of the sample are affected by turning, e.g., the organs of a person. Moving parts are expensive, require maintenance, are heavy and can introduce inaccurate orientations for the source-detector pair, which is harmful due to each projection being compared to another based on their position. Consider that the sample in figure

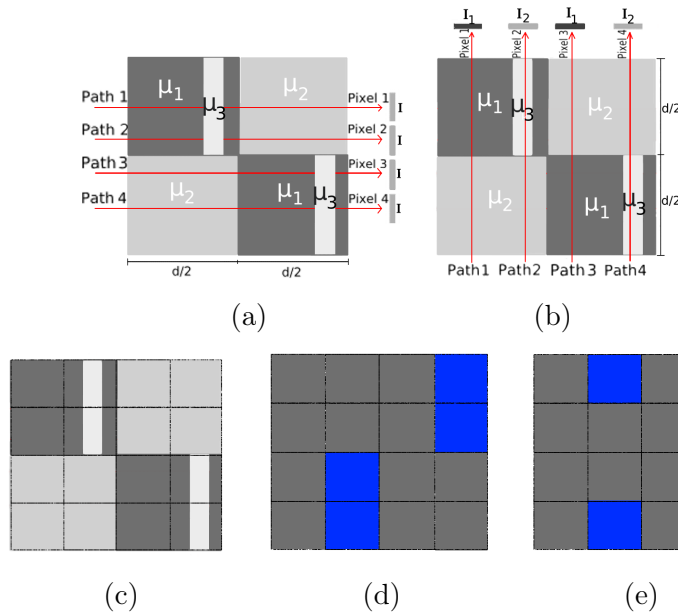


Figure 6: *Example of a simple sample (grayscale rectangles) imaged with X-rays, from two different perspectives and two possible false interpretations of the inner structure of the sample. Image (vertical dashed line) formed in a) is of one value suggesting the sample to be homogeneous. b) shows how sample is heterogeneous, two different pixel values in the image (horizontal line), and with the image a) allows some guesses for the inner structure. For these "measurements" the pixel layout on sample are shown in c) and two false possible interpretations of the sample are shown in d) and e).*

6(a) was measured one pixel too low, but perspective thought to be the same. Now sample would be thought to have one row of pixels with no attenuation,  $\ln(\frac{I}{I_0}) = 0$ , and sample would be thought to be smaller by one row of pixels. This example also highlights how important the precision of motion is, movement of one voxel size can introduce blurring of the constructed image [32]. The problem can be solved by placing multiple source-detectors pairs around the sample, which allows multiple perspectives to be measured at the same time without movement of either the sample or the apparatus, enabling faster and more precise measurements. [32]

For industrial and scientific applications, the studied structures and samples are usually not affected by movement, so movement of them does not affect the CT images. The sample is placed on moving and turning stands, which enables the device to acquire desired perspectives by turning the stand and therefore the sample. Also, the position of the sample can be precisely specified via the movement of the stand. Turning the sample has the same precision requirements as moving the equipment. [32]

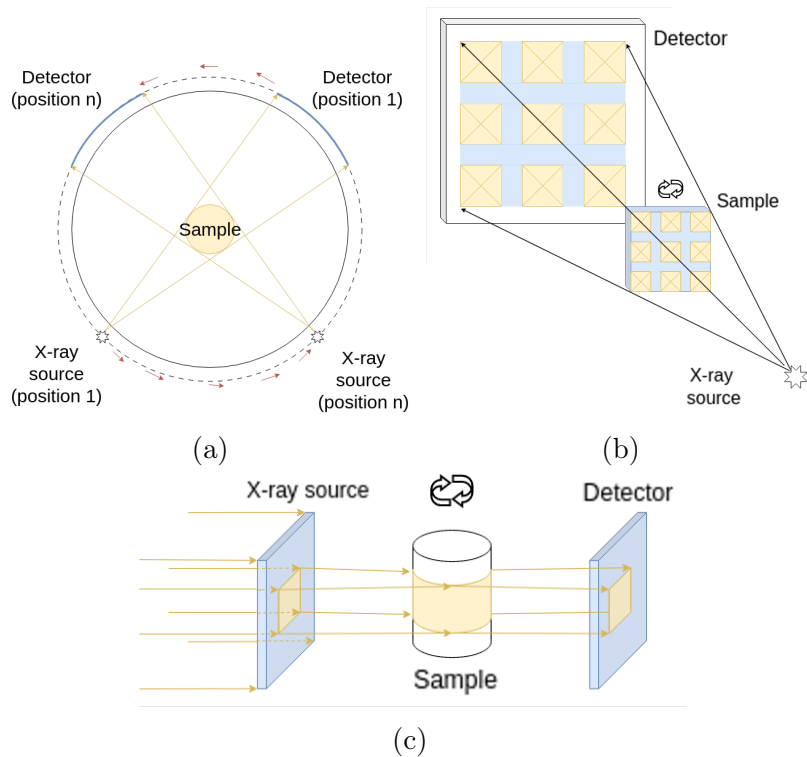


Figure 7: *Illustrations of X-CT setups: a) is a moving configuration, in which sample is stationary and machinery turn around it. At b) and c) the sample is turning and camera and X-ray source are stationary, difference in them coming from different beam shapes. Setup b) has cone beam and demonstrates how linear magnification is possible with cone beams, c) illustrates a parallel beam setup.*

I previously mentioned how the X-ray source affects the spectrum of the X-rays (see section 2.2.2), but it also affects the shape of the beam affecting the X-CT device setup. X-tubes produce a cone-shaped beam (cone beam), which commonly lights the whole sample at once [32]. The further away the sample is from the source, the larger the field of view (FOV) of the cone beam and the bigger the sample can be. Magnification is possible with the cone beam; by moving the detector closer to the sample each pixel on the detector represent smaller volume of the sample making it larger in the images. It decreases the volume each voxel represents [32], and is demonstrated in figure 7(b). Scans done with an X-tube source take from minutes to hours, depending on the resolution [44].

The synchrotron source is further away from the sample than the X-tube, from meters to hundreds of meters, which makes the produced X-ray beam highly perpendicular to the sample, a parallel beam. As a result, the voxel size represents the pixel size of the detector. Due to the synchrotron producing much higher flux

than the X-tube, it allows faster scan times ranging from sub-seconds to minutes [44]. A monochromatic beam is often required for phase-contrast imaging [45], but it is also possible with polychromatic sources [46, 47].

Most commonly, X-CT scanning is based on the attenuation of X-rays. Each X-ray image is a gray value image based on the ratio of initial intensity and penetrating intensity; see section 2.2.5. Different perspectives are taken to determine different attenuation coefficients in the sample, which is how the final 3D image is formed in the reconstruction process, see below. The attenuation method is great for samples with high variation in the contrast of the inner structures and high variance in the attenuation coefficient, like porous rocks and microchips [16–18]. Monochromatic X-radiation is beneficial but not required. Monochromatic radiation can be optimized for the previously mentioned optimal penetration ratio of 14 % . Of course, the ratio can not be optimal for each path the X-rays take. Polychromatic radiation, on the other hand, can not be optimized as well and does not give as good a contrast as monochromatic radiation [32]. This is due to the fact that detectors are normally not suited for energy detection. Attenuation is dependent on the energy of the photon, so quantifying the different attenuation coefficients of each material in the sample from other materials is not so precise [30, 32]. Therefore, with monochromatic radiation, attenuation coefficients can be calculated more precisely which allows for better contrast. Polychromatic radiation can be filtered to reduce the spectrum at the lower energy end, nullifying highly attenuating low energy X-rays, which contribute little at best to the images. It also reduces radiation dose, which is important if the studied subject is alive [43].

Another possibility is to use phase shift-based X-CT device. Like visible light, X-rays experience phase shift while traveling through a material, which they are capable of penetrating [48]. Phase shift-based applications are better suited for samples containing similar attenuation coefficients, in which normal attenuation-based applications perform poorly [32]. Phase-shift can not be measured directly; therefore, detectors measure fluctuating intensities formed by the interference of X-rays in different phases. [32, 45, 49, 50]

### 2.2.7 Reconstruction

The process of forming 3D images from the projections collected during an X-CT scan is called reconstruction. Like previously mentioned, it is done with specific algorithms, of which there are many: filtered back projection, Fourier-domain reconstruction, and iterative reconstruction, to name a few. In this work, I will focus on reconstruction via filtered back projection, which was used in the study. First, I will go over the theory done by Rhadon, expand on it with Fourier slice theorem, and finally expand it into filtered back projection. [42, 51, 52]

Consider a parallel beam source that penetrates the sample at a cross-section, or plane, and the attenuated X-rays hit the detector on the other side of the sample; see the configuration in figure 8(a). Here I will use  $(x, y)$ -coordinates in the plane of interest so that origin coincides with the rotation axis normal to the plane and each point  $(x, y)$  at the plain has an attenuation coefficient of  $\mu(x, y)$  ( $\mu(x, y) \approx 0$  outside the sample). In the plane, the detector can be considered to be a line  $L$  which is perpendicular to linear X-ray paths. Each of the paths can be defined as a line with

$$p_j = x \cos(\theta_n) + y \sin(\theta_n), \quad (13)$$

where  $p_j$  represents the perpendicular distance from origin to the X-ray path and  $\theta$  the direction of the line connecting origin to the X-ray path [42, 51, 53]. Indexes  $j$  and  $k$  are positive integers;  $j = \{1, 2, 3, \dots\}$  and  $k = \{1, 2, 3, \dots\}$ . Configuration is introduced in figure 8(b), where all  $p_1 - p_5$  have the same angle  $\theta_k$ . Notice that each  $p_j$  represents one X-ray path through the sample from one perspective, and each  $\theta_k$  represents one perspective. For given  $\theta_k$  each path  $p_j$  gives one value  $g(p_j, \theta_k)$  in the detector according to attenuation ( $\ln(I_0/I)$ ) through the specific path. The collection of all  $g(p_j, \theta_n)$  with the constant  $\theta_n$  therefore represents a projection. Projections gathered to a 2D image based on their angle  $\theta_n$  is called a sinogram.

By using the theory of Radon from 1917, each intensity  $g(p_j, \theta_n)$  can be written as

$$g(p_j, \theta_n) = \int_{-\infty}^{\infty} \int_{-\infty}^{\infty} \mu(x, y) \delta(x \cos \theta_n + y \sin \theta_n - p_j) dx dy. \quad (14)$$

$\mu(x, y)$  is attenuation coefficient of the sample at point  $(x, y)$  and  $\delta$  is Dirac delta function limiting the integral only on the wanted X-ray path [42, 53]. The equation presented is an analogue of Beer's law in equation (5). A sinogram is now an image, or 2D matrix, made from values  $g(p_j, \theta_n)$  where  $p_j$  and  $\theta_n$  represent corresponding coordinates on the image.

Fourier transform  $G(\omega, \theta)$  of projection  $g(p, \theta)$  is given by

$$G(\omega, \theta) = \int_{-\infty}^{\infty} g(p, \theta) e^{-i2\pi\omega p} dp, \quad (15)$$



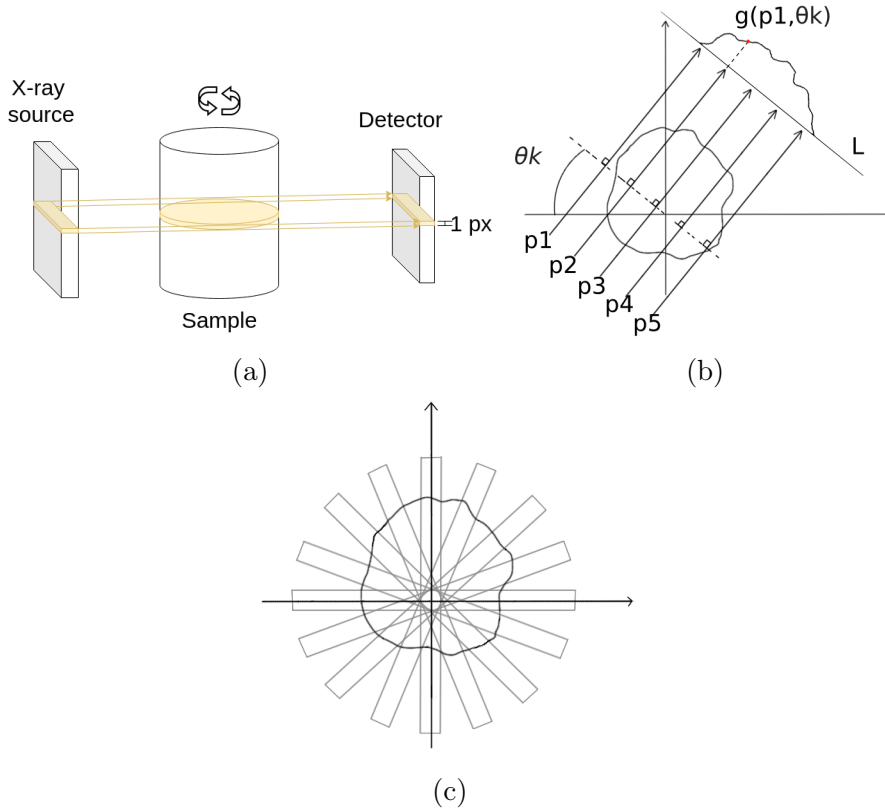


Figure 8: At a) one cross-section of a sample is imaged using at normal X-CT measurement and b) illustrates the matter from different perspective while introducing variables used here. c) demonstrates Fourier slice theory and a simplified image production accordingly. Each rectangle is a slice from which the Fourier transform of the final image is produced.

where  $\omega$  is (angular) frequency [42]. Inserting the equation (14) into the FT and making variable changes  $u = \omega \cos \theta$  and  $v = \omega \sin \theta$  one gets

$$\begin{aligned}
 G(\omega, \theta) &= \int_{-\infty}^{\infty} \int_{-\infty}^{\infty} \int_{-\infty}^{\infty} \mu(x, y) \delta(x \cos \theta + y \sin \theta - p) e^{-i2\pi\omega p} dx dy dp \\
 &= \int_{-\infty}^{\infty} \int_{-\infty}^{\infty} \mu(x, y) \int_{-\infty}^{\infty} \delta(x \cos \theta + y \sin \theta - p) e^{-i2\pi\omega p} dp dx dy \quad (16) \\
 &= \int_{-\infty}^{\infty} \int_{-\infty}^{\infty} \mu(x, y) e^{-i2\pi(x \cos \theta + y \sin \theta)} dx dy.
 \end{aligned}$$

The result is a 2D FT for the attenuation coefficient, meaning that 1D FT is a slice from the 2D FT of the reconstructed image [42]. This result is called Fourier Slice Theorem. A full cross-section image is formed when all of the slices are combined, illustrated in figure 8(c). Each slice go through the center of the cross-section and

their place is determined by the angle  $\theta$ . Unfortunately, the resulting image can be blurry, especially at the edges of the sample. The problem originates from the fact that each slice goes through the center of the cross-section and therefore is over represented while edges are underrepresented, as shown in the figure 8(c) [42, 51].

Fourier-slice theorem can be improved on by continuing on equation 16) and changing into cylinder coordinates with

$$u = \omega \cos \theta, \quad v = \omega \sin \theta \quad \& \quad du dv = \omega d\omega d\theta,$$

where  $\omega$  is presents distance from the origin [53]. Coordinate change yields inverse FT for equation (16) as

$$\mu(x, y) = \int_0^{2\pi} \int_{-\infty}^{\infty} \omega G(\omega, \theta) e^{i2\pi\omega(x \cos \theta + y \sin \theta)} d\omega d\theta \quad (17)$$

which can be reduced knowing that  $G(\omega, \theta + \pi) = G(-\omega, \theta)$  and inserting  $p = x \cos \theta + y \sin \theta$  as

$$\mu(x, y) = \int_0^{\pi} \int_{-\infty}^{\infty} |\omega| G(\omega, \theta) e^{i2\pi\omega p} d\omega d\theta = \int_0^{\pi} g'(p, \theta) d\theta, \quad (18)$$

where  $g'(p, \theta)$  is an inverse FT of projections, which is defined as

$$g'(p, \theta) = \int_{-\infty}^{\infty} |\omega| G(\omega, \theta) e^{i2\pi\omega p} d\omega. \quad (19)$$

This is the inverse FT of the function  $G(\omega, \theta)$  multiplied by a so called filter function  $|\omega|$ . The use of filter gives the name for the reconstruction algorithm filtered back projection. [42, 51, 53]

Now, making a 2D image out of multiple projections has four steps: i) Compute the 1D FT of each projection (or sinogram) ii) Multiply each FT by the filter function iii) Take the 1D inverse FT of all of them iv) Integrate, or in practice sum, over the filtered projections (equation (18)) to get a single pixel of the reconstruction [53]. In the final image, we have effectively solved the attenuation coefficient for each point, which are presented as pixel values  $\mu(x, y)$ .

A 3D image of the sample is acquired via stacking cross-section images. Data for reconstruction is acquired with a detector with multiple lines of pixels, so many cross-sections can be measured at once. If the detector were only one pixel in height, it would be possible to move it to a different height and get the same result. Each cross-section reconstructed represents one slice of the sample with a thickness of one pixel width, which represents projections gathered with one row

of detector pixels [42, 53]. Therefore, each layer of the 3D image can be thought of as a slice of the sample with volume. In my studies, each formed image was  $1976 \times 1976 \times 1976$ , meaning there are 1976 layers of  $1976 \times 1976$  2D images.

Algorithm introduced above is suited for planar X-ray sources. In this thesis I used a cone beam source, in which case the reconstruction algorithm is more complicated but follows the same principle. The reconstruction program used in this work was programmed by A. Miettinen using Pi2Py2 library. The algorithm is based on the filtered back projection algorithm introduced above. For more detail see website [54].

### 2.2.8 Artifacts

Artifacts are defects in the images that do not represent the sample. Sources for the defects are plentiful and can originate from X-ray physics, improperly working instrument(s), or the sample [55]. The magnitude and shape of the artifacts depend on the source of the artifact and the magnitude of that source, and sometimes multiple different sources can cause the same kind of artifact. In this section, I will go over the origin of artifacts, what kinds of artifacts there are, and how to minimize them.

Artifacts can be modeled as a false representation of attenuation inside the sample. Let's consider the cross-section of a sample.  $\mu(x, y)$  represents the real attenuation of the sample at a point  $(x, y)$  and  $\hat{\mu}(x, y)$  the calculated attenuation coefficient after reconstruction at the same point. Images are successful if  $\mu(x, y) \approx \hat{\mu}(x, y)$  but if the variation is too great among the two, there are artifacts at the point  $(x, y)$ . Provided that great variance is the case and is caused by a factor  $\Phi$ , the artifacts are formed via function [56]

$$\Delta_{\Phi}(x, y) = \mu(x, y) - \hat{\mu}(x, y). \quad (20)$$

According to the function above, artifacts can range from effecting only local sections of the image, even one-point artifacts that would be eliminated during filtering in the reconstruction processes, to the whole image.

### Random noise

The most common form of artifact is noise, which is found in all the X-CT images. Originating from the quantum nature of the X-radiation, noise is inevitable and is seen as false pixel values. In other words, the number of photons reaching the detector is fluctuating, making the final image grainy even when there is no sample or the sample is homogeneous. Noise is commonly measured as a signal to noise ratio, and the higher it is, the better. Noise can be mitigated by extending exposure time and increasing photon flux, both of which result in the detected signal being

an average over larger number of photons, thus reducing random fluctuations in it. There are also algorithms to remove noise from the images, and the approach taken in this work is discussed below in Section 2.3.3. [57]

### **Movement artifacts**

I have previously mentioned how important it is to keep the sample and apparatus from moving in unwanted ways. All unwanted movement leads to a blurry image with streaking if there is a lot of movement in multiple projections. On a smaller scale, for example, when only one part of the sample moves in a couple of projections, the artifact is localized on the moved section as incorrect gray values for the voxels and streaks in the final reconstructed image [55]. To minimize movement-based artifacts, machinery needs to be maintained and calibrated regularly. Also, a stable stand for the sample is important, as is the fact that the sample needs to be stable in the time frame of the measurements. Some samples can even be unsuitable for X-CT because X-rays absorbed into the sample can heat it or cause radiation damage, introducing some movement in the structures of the sample [58].

### **Ring artifacts**

Ring artifacts are formed when one or multiple detector pixel(s) measure intensities differently than other pixels. In other words, the measured value is varied despite the photon count being the same [59]. Using Fourier slice theorem the false measured intensity translates into a line in every slice of sinogram, which is seen as a ring in the reconstructed 2D image. This is demonstrated in figure 9(a). To minimize ring artifacts the machinery needs some calibrations and in some cases the detector needs to be replaced [55].

### **Cone beam artifacts**

The geometry of the sample can also introduce problems while imaging. If some sections are visible in some projections but not in others, the partially seen section will cast a shadow into the final image, a phenomenon called a cone beam artifact. This artifact is most common for samples that are not symmetrical and whose source is a cone beam, as demonstrated in figure 9(b). The image seen is exaggerated to demonstrate how the section can be seen from some projections but not from others. Cone beam artifacts can be mitigated by choosing a smaller interest area to measure or moving the sample further away from the detector to increase the FOV. [55, 60]

### **Undersampling and incomplete projection artifacts**

Undersampling originates from a large angular step, which is equal to not enough projections. This leads to streaks and gray-value defects. An extreme example of

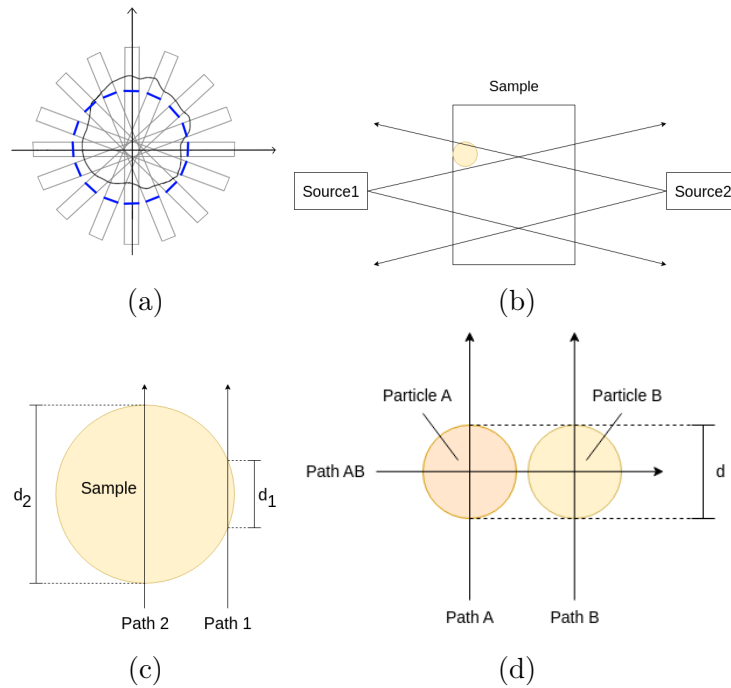


Figure 9: Image a) shows where ring artifacts are shown using the Fourier slice theorem. Object in the middle is the sample, from which the reconstruction image is formed with the 1D slices represented by the rectangles. Each slice has a line in them at the same spot yielding a ring artifact in the reconstructed image like seen in the image. Images b), c) and d) represent situations where artifacts are usually encountered. Image b) has a exaggerated situation in which a cone beam artifacts are formed. Particle with higher attenuation coefficient than rest of the sample is seen as color and the particle is seen by only one of the sources, which lead into an artifacts. Cupping artifact formation is shown in c) which originates from the difference in the two paths lengths  $d_1$  and  $d_2$ , where  $d_1 < d_2$ . Image d) has a situation where 2 particles A and B with different attenuation coefficients are aide by side. Streak and dark band artifacts are formed because one of the particles harden the beam more than the other.

this was demonstrated in the section about X-ray imaging (section 2.2.5) where I only took two projections and could not identify even a simple interior structure of the sample introduced in figure 6. The lack of projections led to insufficient data to reconstruct the images, which is why the artifacts were formed. Simple solution is to take more projections with smaller angular step between them. [55].

Somewhat similar to undersampling are incomplete projection artifacts. The sample does not fit entirely inside the FOV, leading to streaks and gray value defects in the images. Like with undersampling, the computer does not have enough data to reconstruct a good presentation of the sections from which the data is insufficient [55]. Larger FOV can solve the problems, and some algorithms are also made to reduce the incomplete projection artifacts [55]. It is also important to place the sample in the middle of the rotation axis to prevent some parts from being outside the FOV in some projections.

### **Beam hardening**

Beam hardening is an example of a physics-based artifact. Reconstruction programs are usually grounded on the fact that the X-ray source is monochromatic, but in most cases it is polychromatic. I have previously mentioned how the attenuation coefficient depends on the energy of the X-radiation in addition to the material of the sample. For polychromatic radiation, this leads to a situation where low energy radiation does not penetrate the sample and the high-energy X-radiation penetrates with minor attenuation; in other words, the X-ray beam hardens [55, 56, 61–63]. There are two types of artifacts created by beam hardening: cupping artifacts and streak and dark band artifacts [55, 61]. Lets first look how the the beam hardening affects the measurement, then the two special cases, and lastly, how to reduce beam hardening. This section also explains why monochromatic radiation is ideal for X-CT.

Because the low-energy X-radiation attenuates almost completely, it does not affect the measurements. The problem with this is that depending on the path length and the varying attenuation coefficient along the path, the beam hardens varying amounts. Because small-energy X-radiation attenuates strongly, paths that harden X-rays less will have relatively higher attenuation, leading to higher calculated  $\hat{\mu}(x, y)$  [55, 61–63]. Highly hardening paths in turn have relatively low attenuation, resulting in lower  $\hat{\mu}(x, y)$ .

Cupping artifacts are one variety of beam hardening artifacts. Artifacts are seen in the images as brighter edges and darker middle parts in cylinder shaped and other round samples [55, 56]. Paths near the edges are shorter and therefore harden the beam less than the longer paths through the middle of the sample, as demonstrated in image 9(c).

Coupling artifacts form in all samples but are more relevant in mostly homogeneous samples, contrary to streak and dark band artifacts, which are found in highly heterogeneous samples. Like the name implies the artifacts are streaks and dark bands in the final images. Streak and dark band artifacts are most common between two denser materials with different attenuation coefficients [55, 56, 61]. The beam hardening difference between the paths is now caused by a difference in attenuation coefficients, contrary to coupling artifacts where it was caused by a difference in path length [55, 56].

Beam hardening is present in all measurements and cannot be fully disregarded for any polychromatic sources [55, 61]. To minimize the beam hardening artifacts, a pre-filter is often used [55, 56, 61]. Filter hardens the X-ray beam before it hits the sample, therefore minimizing the amount of lower-energy X-rays effecting the measurements negatively. Raising the voltage used to generate X-rays can also help, but it also requires filtering. Other possible methods are cutting the sample so that the high-attenuating particles are not there to effect the imaging, changes in the reconstruction process, and filtering [55, 61, 64].

### **Photon starvation and metal artifacts**

As has been previously mentioned, highly attenuating particles can introduce cone beam and beam hardening artifacts, but they can also form star artifacts due to photon starvation [55]. When almost all of the X-rays are absorbed into the sample, the detector does not get a good signal due to a lack of photons. If there is no signal among all of the projections, the acceleration voltage is too small. Photon starvation is found when a sample contains a very strongly attenuating particle compared to the surroundings, like metal particles, or a large strongly attenuating particle, like bones, which X-rays penetrate longitudinally [55]. Each projection has a strong, dark spike under the highly attenuating particle. The problem in that is that measured projections that have strongly attenuating particles in them do not have any information along the paths along which the strongly attenuating particles lie, leading to bright streaks in the final image called star artifacts [55, 65, 66]. Streaks from star artifacts can also be long and effect large areas of the reconstructed image [55].

Like all artifacts originating from highly attenuating particles, photon starvation can be limited by increasing the acceleration voltage; also, extending the exposure time helps. Both will increase the number of photons detected through the dense particle, giving some information about the area. There are also multiple different algorithms and filtering systems designed to minimize the effect of the artifacts [64–66]. Some systems implement different acceleration voltages used during the imaging process to get better projection data. [55]

## Artifacts in this work

Naturally, some artifacts were found in my images, like photon starvation, beam hardening, movement, incomplete projection, and ring artifacts. Most of the samples fit into the FOV, so there were only two batches with incomplete projection artifacts, and I ensured that the number of projections was sufficient for high resolution images. Photon starvation and movement artifacts imposed the most problems in the study. I will return to the problems in more detail in the Results section.

## 2.3 Measurements and image analysis

### 2.3.1 Device used

A single propellant grain is about 1 mm wide particle. Because of its small size, the used X-CT equipment needs to be able to distinguish micrometer-scale details inside the sample. Micro-X-CT devices are developed for this purpose. They are mostly similar to normal X-CT apparatus but have a smaller beam spot in the X-ray source and detectors that are capable of gaining signal with lesser amount of X-radiation [32, 67].

In this work, I used the Xradia MicroXCT-400 at the University of Jyväskylä. It is capable of approximately 1  $\mu\text{m}$  resolution. The sample stand is the moving component in the measurements, and like previously mentioned, the source was an X-tube with a tungsten target, the Hamamatsu L9421-02 Microfocus X-ray source, which I used at 60 kV. The gained beam is a cone beam that hits the CCD camera (detector), Andor DW436-BV-550. Detector is a digital 4 megapixel, 16-bit camera with five objectives: 0.5X, 4X, 10 $\times$ , 20 $\times$  and 40X.

In this work, I used 20 $\times$  and 10 $\times$  objectives in my measurement, 10 $\times$  on the bigger grains of N5, H7 and H8-batches, 20 $\times$  on the others. The rest of the parameters used in the measurements are introduced in table 1. Note that background images for flat field corrections are taken before, at the middle (after 1001<sup>th</sup> projection) and after all of the projections. I had the X-ray source preheated before the actual measurements, which took 15 minutes to ensure the stability of the X-ray spectrum emitted by the source.

### 2.3.2 Sample preparation

Previously, I mentioned what types of propellant were used and how they were manufactured, simple geometries, basic composition, and the relevant components. I also went over the setup for the measurements but have not explained how the



Table 1: *Parameters used in micro X-CT measurements. Background images were taken three times during the measurements, before, at the middle (after projection 1001) and after the measurements.*

Source distance	21 mm
Detector distance 20× (10×)	2.5 mm (10.5 mm)
Exposure time	15 s
Number of projections	2001
Number of background images	30

samples were chosen and prepared for the measurements. In this section, I will go over grain selection and the sample preparation process for the samples.

I had two different types of samples: normal grain samples and reference samples. A normal grain sample was just a propellant grain glued with superglue on the tip of a carbon rod, as seen in figure 10(a). A minimum amount of glue was used to prevent it from absorbing into the grain and plugging pores or holes. The rod was also polished from the tip so that the glue would grab on to it better with a lesser quantity needed. The grains I used were all relatively upright, meaning that the grain top is perpendicular to the middle of the grain. Tilted grain would have been harder to get inside the FOV in the micro X-CT at 20× magnification due to the edges of the top and bottom being further away from the center of the grain and the rotation center. For each batch, I prepared two grains to get basic information about variance within a batch.

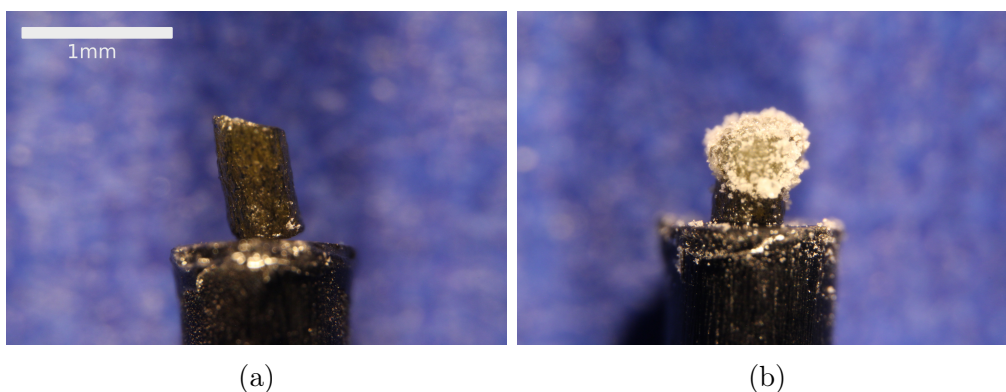


Figure 10: *A microscope image of a) a grain sample from batch N1 and b) a reference sample of  $KNO_3$ . Scale bar in image a) is for both images.*

Reference was made to identify particles with higher attenuation than NC from the samples. Four of the 18 batches measured had only one distinguishable different particle or material phases with higher attenuation than NC; others had two or

more. Most of them could be identified with the method of elimination, but to be sure, some reference samples were made to ensure the results. The chosen reference samples were  $\text{KNO}_2$ ,  $\text{K}_2\text{SO}_4$  and  $\text{KC}_4\text{H}_5\text{O}_6$  and one reference sample was made from each.

All the references were measured in the form they are introduced in the manufacturing process: a fine powder much smaller than a grain of propellant. Unfortunately, powder is hard to measure on its own, especially with the assumption that the powders will introduce some beam hardening and artifacts with the used parameters. This is why reference samples consist of a normal grain sample on which the fine reference powder is glued (see figure 10(b)), allowing the measured powder to be surrounded by the same environment as it would have inside the grain, reducing artifacts. The grain used as the base was from the batch with the smallest grains studied here, N1, allowing all of the reference powder to be inside FOV. A sample made out of batch N1 is also presented in the figure 10.

### 2.3.3 Image analysis

I did analysis with Python code utilizing the following libraries: Sys, Numpy, Matplotlib, Tabulate, CSV, Pathlib, and Pi2 [68–74]. The script is shown in Appendix A. Pi2 is library designed for processing and analysis of terapixel-scale volume images and can be used in languages like Python and C/C++ as a standalone executable [74]. Here I used Python because I am most familiar with it and because it is one of the most widely used scripting languages. A. Miettinen had previously written a similar Python script, and I used that as a basis for my script. The analyzed images were grayscale images of propellant grains made with X-ray tomography. Samples consisted of nitrocellulose (NC) mass, which took most of the grain mass, pores, holes, and denser particles. Script does not separate pores and holes from each other, so when referring to pores, I refer to pores and holes at the same time. Simply put, the script i) denoised the sample image; ii) made the sample image binary, separating NC mass from pores or denser parts and background; iii) calculated pore diameters and pore-to-pore distances, iv) calculated porosity; and v) saved distance and diameter data to .csv format.

### Image cropping and denoising

First, the original reconstruction was cropped in the z-direction (parallel to the injection direction in the manufacturing process) such that the entire cylindrical cross-section of the sample was visible in the first and last slices. This was important because code could not always realize where the propellant grain starts and ends in the z-direction, introducing inaccuracies in analysis. The next process

was denoising, which was made by defining the function *denoise* that attenuates imaging noise by using a bilateral filter [74].

Bilateral filter takes a weighted local average over the all of the image pixels  $r_i$ , where weight value depends on the spatial and radiometric attenuation functions  $S$  and  $R$ , respectively. Mathematically, bilateral filter  $I'(I, x)$  is expressed as [75, 76]

$$I'(I, r) = \sum_{r_i \in \Omega} I(r_i) S(r_i, r) R(I(r_i), I(r)), \quad (21)$$

where  $I(r)$  is the original image at a point  $r$ , and  $r$  and  $r_i$  are coordinate points  $((x, y, z))$  in a set  $\Omega$  containing all of the points in the original image. Both functions  $S$  and  $R$  are defined as Gaussian functions

$$\begin{aligned} S(r_i, r) &= e^{-\frac{1}{2} \left( \frac{|r_i - r|}{\sigma_S} \right)^2} \\ R(I(r_i), I(r)) &= e^{-\frac{1}{2} \left( \frac{|I(r_i) - I(r)|}{\sigma_R} \right)^2}, \end{aligned} \quad (22)$$

where  $\sigma_S$  and  $\sigma_R$  are standard deviations for spatial and radiometric attenuation, respectively [75]. Denoised image is therefore calculated as an average over all the image pixel with two Gaussian weight values taken into account, yielding filtered image with less noise without loss of sharp edges [75, 76]. Sharp edges are commonly lost if image is only filtered with spatial filtering.

## Segmentation

Thresholding was done so that the images were made binary (separate two phases in the image, like background and NC mass). Thresholding process determines if a pixel  $I(x, y, z)$  at a point  $(x, y, z)$  is in a phase wanted phase by comparing it into a threshold  $T$ , determined here with ImageJ. If  $I(x, y, z) < T$  pixel value is set to 0 and if  $T < I(x, y, z)$  pixel value is set to 1. Separating NC mass from pores was achieved using threshold  $T_p$  to give the image  $I_p$ , seen in figure 11(b), which is made from image 11(a). From the thresholded image the islands with pixel value 0 surrounded by pixels with value 1 are closed and have value 1, forming a mask image  $M$ , shown in figure 11(c) [77].  $M$  is an image similar to  $I_p$  but does not have pores represented in it, and therefore  $M$  represents the full volume of the grain. Dense particles are separated by using a higher threshold  $T_d$  on image  $I(x, y, z)$  and then the gained image is subtracted from image  $M$ , yielding binary image with NC and pores as 1 and dense particles as 0, seen in figure 11(d). Lastly, all formed images were saved to a designated folder as I, thresholded image, and M, mask image. In this thesis, I will be using  $I_p$  and  $I_d$  to refer to images made with thresholds  $T_p$  and  $T_d$ , respectively. All three images are used to separate different areas from the grain and are therefore referenced multiple times by other functions introduced later. [74]

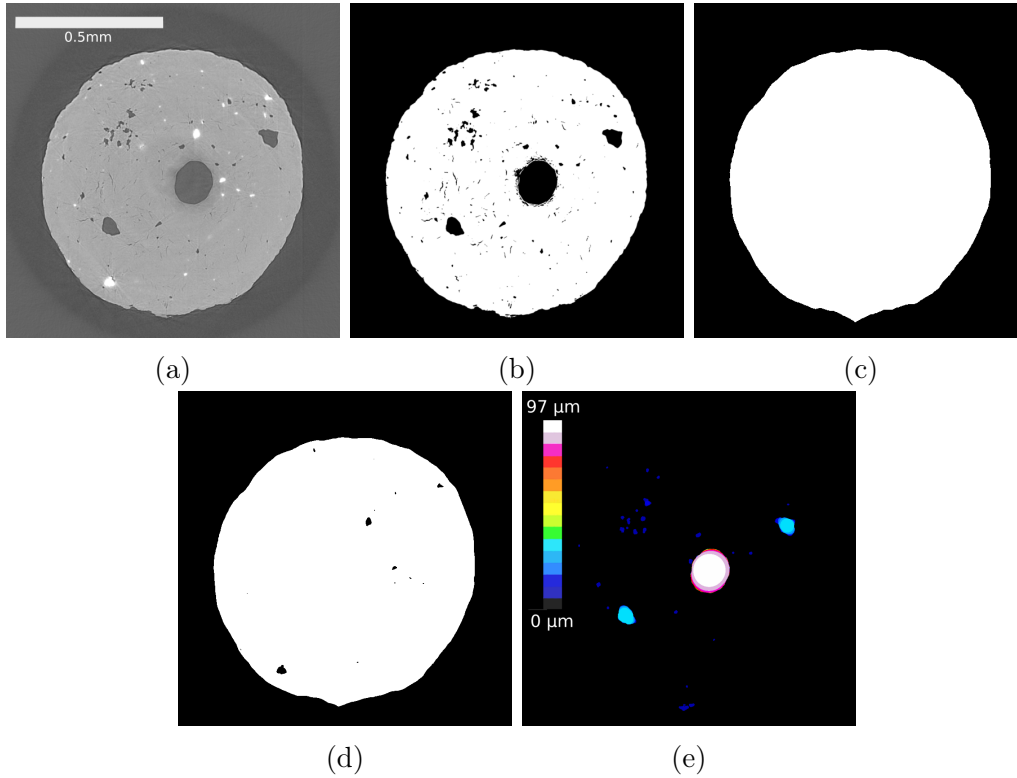


Figure 11: A cross-section of batch  $N_4$ , in a), and all of the images which the python script forms and saves during the analysis. b) is thresholded image and holds all the pores in it as dark spots while d) is the same but for dense particles. Mask  $M$  in c) is made from b) and defines the borders of the grain during the analysis. Finally e) is thickness map image holding all spheres fitted inside the pores in image b). Scale in image e) shows what size the spheres are in the image.

### Calculating pore diameter and distances, and dense particle diameters

The next two functions work similarly but calculate three different parameters depending on the given parameters: pore size and distribution of the sizes (function named: *pore\_diameter*), dense particle size and distribution of the sizes (function named: *pore\_diameter*) and material distances between pores and the distribution of the distances (function named: *wall\_diameter*). The more simple of the two is the so-called wall diameter calculation, which calculates the local thickness maps of  $I_p$  or  $I_d$ , depending on the given parameters, example of thickness map is seen in figure 11(e). There are two possible algorithms to choose from when running the script [74]. Introduced in [78] is the slower one of the two, but it requires less Random Access Memory (RAM) [78]. Faster and more RAM demanding algorithm is introduced in [79]. The faster algorithm is set as default, but if the script can not

complete a run due to insufficient RAM, the algorithm is changed to the slower one. Next, I will go over the two algorithms used to make the thickness map, starting with the memory saving one called Hildebrand-Rüegsegger algorithm (HR) [78].

Local structure thickness  $\tau(p)$  at arbitrary point  $p$  inside set  $\Omega \subset \mathbb{R}^3$  is defined as [78]

$$\tau(p) = 2 \cdot \max\{r | p \in B(x, r) \subseteq \Omega, x \in \Omega\}. \quad (23)$$

Here  $B(x, r)$  is a set of points inside a sphere with a center  $x$  and radius  $r$ , and  $\Omega$  represents a segmented pixel set, whose local thickness need to be determined. Local thickness is therefore defined as the biggest diameter of the largest sphere, which contains point  $p$  and is inside the studied structure  $\Omega$  (pores, denser parts, or NC mass). The mean thickness of the structure is defined as

$$\bar{\tau} = \frac{\iiint_{\Omega} \tau(x) d^3x}{\iiint_{\Omega} d^3x}. \quad (24)$$

Equation 23 can be transformed into a more practical form by using the distance map  $D$  which is defined as the radius of the largest sphere centered at the point  $q \in \Omega$  and still completely inside the structure  $\Omega$ , i.e., distance from  $q$  to the edge of the set  $\Omega$

$$D(q) = \max\{r > 0 | B(q, r) \subseteq \Omega\}. \quad (25)$$

Now the equation (23) can be transformed into

$$\tau(p) = 2 \cdot \max_{q \in X(p)} (D(q)), \quad (26)$$

where

$$X(p) = \{x \in \Omega | p \in B(x, D(x))\} \quad (27)$$

is the set of centers of all spheres that contain  $p$  and whose radius is determined by the distance map. Here, the calculations leading to the local thickness map are split into two steps: i) Calculation of the distance map using the equation (25). ii) Calculation of the thickness map with equation (26). The second step would lead into great RAM demand with equations (26) because of the sphere inclusion test in (27). The problem can be decreased by defining the distance ridge as the set of the center points of all non-redundant spheres

$$\Omega_R = \{p \in \Omega | B(p, D(p)) \not\subseteq B(x, D(x)), p \neq x, x \in \Omega\}, \quad (28)$$

and redefining the set in equation 27 as

$$X(p) = \{x \in \Omega_R | p \in B(x, D(x))\}. \quad (29)$$

In addition, approximation that  $\Omega_R$  is  $\Omega$  without spheres that are totally under the neighboring voxel spheres is required, making defining  $\Omega_R$  easier. This makes defining  $\Omega_R$  easier than the calculations with equations (25) and (27), which would not be the case without the approximation. Now only spheres that are not part of other spheres are tested. Calculations of distance ridge can also be done efficiently on discrete data when doing inclusion tests only for the neighboring voxels.

Distance map can be transformed into a thickness map into a blank image by drawing each sphere determined by distance map so that the diameter of the sphere is represented by the drawn shade and so that smaller diameters can not replace larger ones. This is shortly what HR does. Faster operation time can still be achieved by separating each dimension to be calculated separately, like presented in [79]. This is achieved by marching from the sphere center into positive and negative x-direction until the edge of the sphere is encountered at a distance  $R$  and for each pixel location  $x$ , a squared extent of the sphere in y-direction is saved in temporary image T as

$$r_y^2 = R^2 - |x - c_x|^2. \quad (30)$$

Like above,  $c_x$  is the sphere's center coordinate in the x-direction. The same step process is continued in the y-direction while the squared extent of the sphere in the z-direction is saved into the temporary image T as

$$r_x^2 = r_y^2 - |y - c_y|^2. \quad (31)$$

Note that local extent  $r_y$  is considered the radius in the yz-plane. Finally, the step process is done in the z-direction, where  $r_z$  determines the ranges of pixels that are colored with value  $2R$ . Process described above is for a single sphere but in addition, multiple spheres can be drawn at the same time. [79]

For multiple different-radius spheres, the drawing is made even faster by skipping spheres that are inside other spheres, as they are redundant. These logics are different for each dimension, and I will not go over them here. The algorithmic improvements on HR make the calculation of thickness maps fasted in exchange for higher requirements for RAM [79].

Local thickness map is also used to determine pore diameters, but first pores must be separated from the background; both have pixel values of 0. Mask  $M$  is used to help with this. All of the pixel values in the mask are switched from 0 to 1 by the function pi.linmap. Here pixel value of the mask  $M(x, y, z)$  is changed to  $M_l(x, y, z)$

$$M_l(x, y, z) = 1 - M(x, y, z). \quad (32)$$

Adding the new image  $M_l$  with either image  $I_p$  or  $I_d$  we get a sum image containing pixel values of 0 in pores or dense parts and 1 everywhere else. Using operation

similar to (32) on the sum image, we get an image where only pores or denser parts have value 1. Now local thickness map can be used to determine pore/hole sizes similarly to wall diameters. Both diameter-determining functions save thickness maps with specific names so that they can be referenced later.

Images  $I_p$  and  $M$  are also used to calculate the porosity of the sample, with a defined function named *porosity*. First, we need the number of pixels that contain NC  $N_m$  that is calculated by summing all values of  $I_p$ . The total number of pixels inside the outlines of the propellant grain  $N_f$  is gained by summing all the values of  $M$ . Porosity  $\phi$  is defined as the total volume of the pores related to the total volume of the object, which can be expressed with pixel counts as

$$\phi = \frac{N_t - N_f}{N_t}. \quad (33)$$

### Calculating and saving histogram data

The next defined function in the script calculates the normalized distribution of the diameters using previously saved thickness maps for all diameter types. The function doing this is called *calc\_distr* and it saves the data as NumPy arrays at variables `data` and `bin_starts`, which contain histogram counts and bin position, respectively. The count value corresponding to the first bin is changed to 0 because all of the background pixels are at the first bin, and now the output data gets nicely scaled automatically for possible plotting of the data. Bin edges are multiplied by the pixel size of the sample and changed so that they represent the center coordinates of the bins. Count data is normalized by dividing every point in the data by the integral over all the data points. The function for calculating the normalized data returns centered bins and normalized histogram data, which are referenced by the last function, *diameter\_distributions* to calculate mean values of pore diameters, dense particle diameters, and wall diameters. Mean values are calculated as weighted average for centered bins where histogram data points form the weight for each point. The last function also collects normalized histogram data into the csv file `raw_data`.

### Running the script

All functions introduced in this section are called in the proper order by one main function called `run` function. Parameters used in the `run` function are introduced in table 2 with their respective default values and data types. The `run` function collects mean data and saves it into a csv file `mean_data`. The script can not run multiple analyses at the same time, and every run took from 30 minutes to 8 hours (depending on the hard drive and if denoising was necessary, it could take longer if used with a slower hard drive), so I called `run` functions from separate

scripts, made for each sample, and ran them all back to back from the terminal. This allowed me to not wait for each analysis to end and start the next.

Table 2: *Python script parameters used in each function defined at section 2.3.3.*

<b>Variable [Default value]</b>	<b>Description</b>	<b>Data type</b>
sample_name	Name of the sample in the folder the script is ran from.	string
threshold1	Pixel value to separate pores from NC mass.	real number
threshold2	Pixel value to separate denser parts from NC mass.	real number
pixel_size	Pixel size in $\mu\text{m}$ .	real number
run_type ["pore"]	Determine what will be separated.	strings: "pore" or "dense"
closing [130]	Diameter which determines how big holes are closed while making mask.	rel number
folder ["/"]	Folder in which one want to save the images formed.	string
tmap_mode ["False"]	Change to less RAM demanding thickness map algorithm	Boolean: (True/Fanse)



### 3 Results

The process in this study was simple: I prepared the sample and used the parameters introduced in the table 1 to gather projection data. Projection data was reconstructed using the in-house developed reconstruction program, introduced in section 2.2.7. Finally, the 3D images were analyzed using the Python code introduced in Section 2.3.3, and qualitatively by visual inspection. I compared images inside the same batch (two images from each batch) and variety while also comparing differences between each batch and variety. Like previously mentioned, images from reference samples were used to confirm all the clearly separable phases of the images.

I will first go over the different phases found inside propellant grains and what their identities are. Then I will evaluate the image quality and how well different phases can be separated from each other while also considering the artifacts found in the images. Lastly, I will review the results acquired via script and compare them with the materials used to produce each of the samples.

#### 3.1 Material phases visible in the images

Each grain is composed of three to seven phases, which are highlighted and numbered in figure 12(a) and 12(b). Naturally, the majority of the volume of a grain is NC in all cases, marked as number 1 in figure 12(a). Numbers 2 and 3 represent pores and the middle hole in the image, which are separated from each other because batches N6-N8 do not have a hole going through them but are highly porous, see figures 12(c) and 12(d). Pores and holes are, however, seen with similar pixel values equal to the pixel value of the background. Particles marked as 4 in figure 12(a) are slightly more attenuating than NC, while 5 and 6 are much more highly attenuating particles compared to NC. Both 5 and 6 cause beam hardening and star artifacts in the images, but 6 produces more severe ones. The main difference between 5 and 6 is seen in the pixel value, which is for 5 around 50 000 (variation is high) and saturation point 65 535 for 6. The composition of 7 is different from the other highly attenuating particles. It resembles more of a web with small particles attached to it. Some grains also had some glow on the edges, which I concluded to be the same substance as 7, which I will be returning to below.

NC was easy to identify due to its being the main ingredient of N-type, HE-type, and two-component propellants, and therefore it is seen in all of the images as the most common phase. Holes and pores are also obvious in the images, as they have the same pixel value as the background. This is also expected due to there being only air inside of them, like around the grain in the measurement chamber, yielding the same attenuation coefficient for pores, holes, and background.

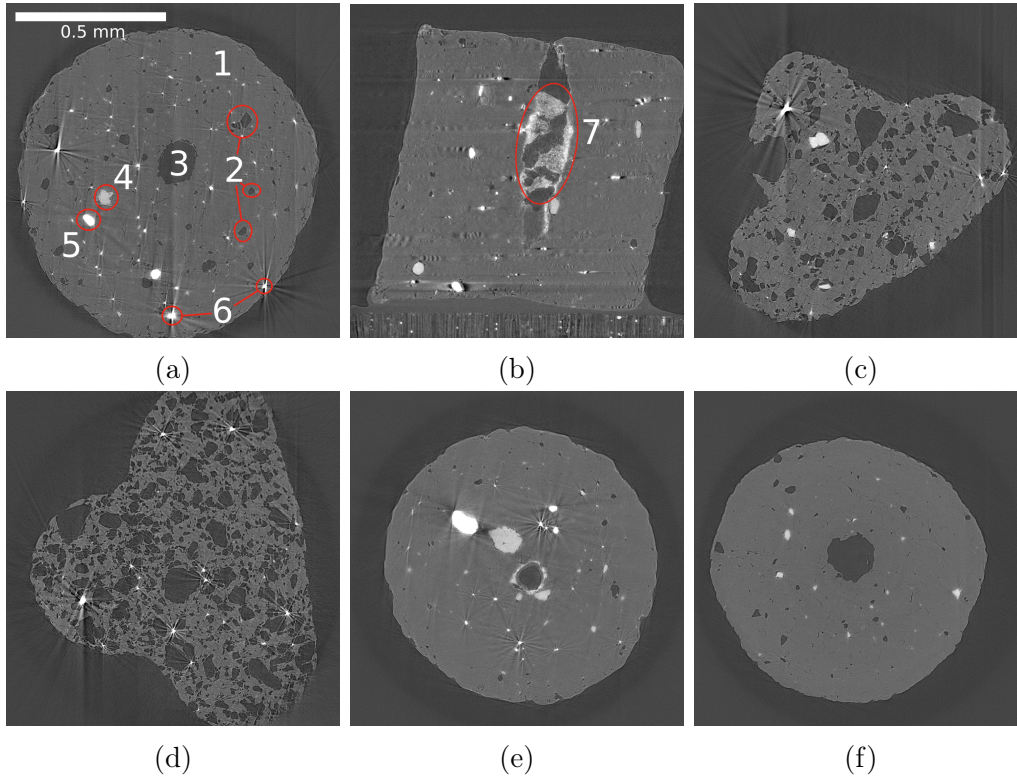


Figure 12: Cross-sections from the completed CT images, where a) and b) highlight and number the different phases seen. Image a) is a grain from batch H5 and b) is a grain from H1. Scale seen in a) is the same for all images. Images c) and d) are grains from batches N7 and N8, respectively, and demonstrate more porous grains without middle holes. Image c) shows also a grain from H1 demonstrating how all of the identified phases can be found in one sample and how large  $K_2SO_4$  particles introduce beam hardening artifacts. Image f) being a grain from batch N3 does not have any metal particles in it. Images a) and c-f) are cross-sections from at horizontal plane while b) is from vertical plane.

For all the particles more attenuating than NC (4, 5, and 6 in figure 12(a)) the identification was achieved via the process of elimination, and in the cases of 4 and 5, I made three reference samples to verify the conclusion. Particles marked with the number 4 are identified as potassium bitartrate  $KC_4H_5O_6$ .  $KC_4H_5O_6$  is a component used in the production of all the batches in this study except N6 and N7. This is also seen in the images. Images of grain from N6 and N7 batches do not have particles with similar pixel values as in all the other images, which are similar to particles marked as 4 in figure 12(a). This was further confirmed via the reference sample seen in figure 13(a), where particle size and pixel values correspond to the sizes and values seen in grain images.

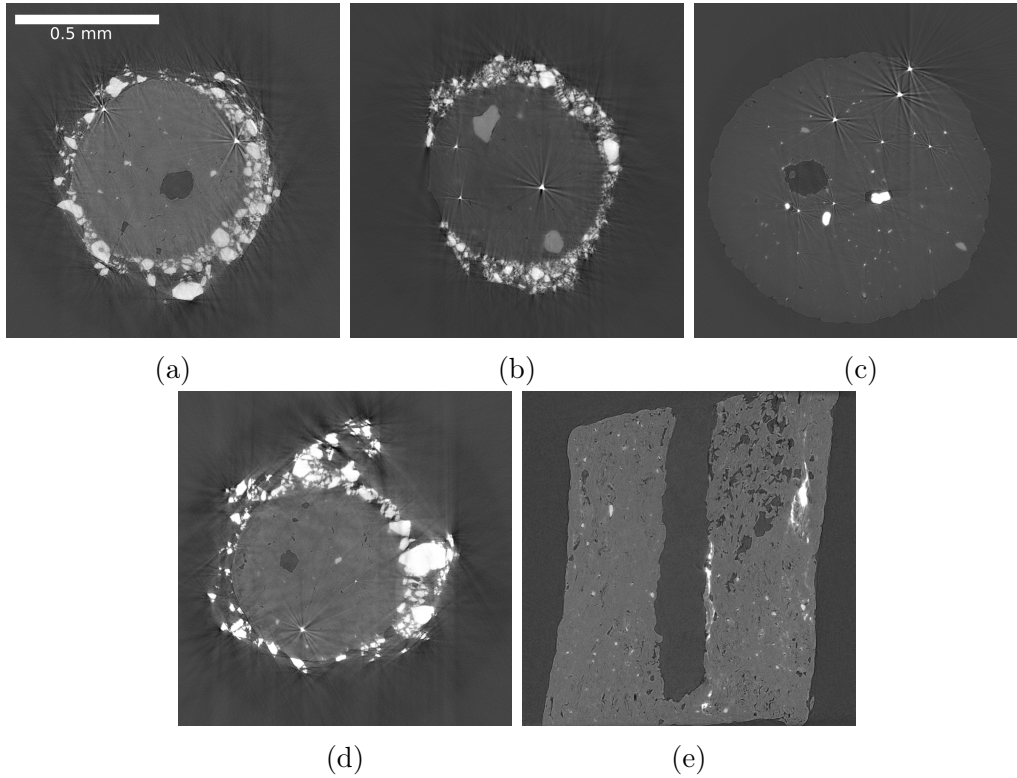


Figure 13: *Acquired images from the reference samples and two grains from batches H1 and T1 as follows, a) is  $KC_4H_5O_6$  reference, b) is  $K_2SO_4$  reference, c) is the grain from batch H1, d) is  $KNO_3$  reference and e) is the grain from batch T1. Note that scale bar seen in a) is for all images and that image e) is a vertical cross-section and others are horizontal. Images b) and c) are made with different reconstruction parameters and forced to look similar with contrast manipulation.*

Highly attenuating particles marked as 5 are found in the images of grains from batches H1-H8, in other words, all of the HE-type batches in this study. Even though the main difference between N-types and HE-types is the inclusion of NGL in HE-types, the particles can not be from it. NGL consists of the same elements as NC and does not have a highly different density from NC; therefore, NGL can not be distinguished from NC with the used measurement parameters [80, 81]. HE-type batches have another common component not found in other studied batches, which is  $K_2SO_4$ . Unfortunately, images from  $K_2SO_4$  reference sample were unsuccessful, having a lot of beam hardening artifacts and likely some movement during measurements. I tried to measure the sample twice, but the results were even worse. Also, the cupping artifacts of the images were so strong that reconstruction needed to be done with some corrections, which, in order to compare the reference to the grain sample, required a reconstruction of one grain image with

the same corrections. An image of the reference sample can be seen in figure 13(b) and the grain from H1 batch reconstructed with the corrections in figure 13(c). Particle size can be confirmed to be equal to the particles seen in images of grains, but the pixel values vary widely in the reference sample. Note that I changed the contrast of figure 13(b) in a way that it looks more like figure 13(c), meaning that the apparent similarity is only artificial. However, this change in contrast indicates similar relative attenuation between the reference sample and the grain sample. In addition to this, in my opinion, matching particle size and the process of elimination alone confirm the particles to be  $K_2SO_4$  on the basis that there are no other common components with equal particle size between the H1-H8 batches. It is also notable that the reference sample of  $KNO_3$ , introduced in figure 13(d), had particles with suitable particle sizes and a little lower pixel values than seen in the images of grains. However, it is not used in the production of H4-H8 batches. This excludes  $KNO_3$  from being considered as number 5 from figure 12(a).

Like mentioned above, the most clear star artifacts seen in the images are due to particles marked as 6. These are therefore the densest and most attenuating particles in the grains. Star artifacts are seen in all of the images except in the images of grains from N3 and N5 batches, grain from N3 is seen in figure 12(f). N3 and N5 are the only batches without Sn and Bi which are metals with atomic numbers 50 and 83, respectively. Like demonstrated by the equation (4) a high atomic number correlates with a higher attenuation coefficient, and therefore the very highly attenuating particles inside the material can be considered metals Sn and Bi. Identification between them is impossible with the used parameters due to almost all of the X-rays being attenuated while traveling through either of the two materials.

The web like structure of 7 in figure 12(b) indicates that it is not a powder used in the production of propellant but a liquid or substance inserted as a liquid and then solidified. Most of the web like substance is located inside the middle hole. This was an important finding due to it partially blocking the middle hole, which is important for the burning of a propellant, as mentioned in Section 2.1. Depending on the substance, it could lower or heighten the burning speed of the propellant. Middle hole blockage was found in varying amounts in some of the HE-types but not in N-types or two component propellants. In my research, I concluded it to be the same substance that is also inserted on the surface of all the HE-types, SFC. SFC is inserted as a liquid substance after NGL at the same reactor and then dried out, which could make it possible for SFC to migrate into the middle hole and block it as it dries out. However, stagnation is grain-specific and often local, and some of the grains have little to no stagnation inside their middle hole (see figure 13(c)).

First, I considered that NGL could also cause the stagnation of the middle hole without considering the elements in NGL and its density. This led to the production of batch H2. H2 goes over the normal HE-type production process but does not go over the NGL addition. Removal of NGL did not totally remove the stagnation of the middle hole but reduced it significantly. However, this does not mean that NGL plays a role in stagnating the middle hole due to the large grain specificity of the stagnation. For example, grain 1 from H3 grains had SFC for almost the whole hole length, but grain 2 had only a minor amount at one of the openings, not shown. The same was also true for batch H1.

The two batches of two-component propellant were the only batches for which I did not have full knowledge of the recipe. Unfortunately, this led to the situation that I could not identify the phases seen only in them. The undefined phase shown in figure 13(e) is similar to SFC in a way that it does not look like a grainy particle but could possibly be malleable. Phases are located randomly inside the NC mass of the grains and have a higher pixel value than SFC, so they can not be SFC.

### 3.2 Quality of images

The inner structure of the grains is seen with high precision and with good contrasts, enabling sufficient phase separation. Pixel sizes for cross-sections range from  $0.5951\ \mu\text{m}$  to  $0.9051\ \mu\text{m}$  given by the  $\mu\text{X-CT}$  device. A larger pixel size was used for images of grains from batches N5, H7 and H7 via a  $10\times$  magnification camera, contrary to the  $20\times$  in all of the grains from other batches.

The quality of the images was heavily impacted by the components in the grains. Grains from batches without  $\text{K}_2\text{SO}_4$ , Sn and Bi had the least artifacts in them, and grains containing all three had the most artifacts. For example, figure 12(f) illustrates an image taken from batch N5, which does not contain any of the three and has very well defined phases with very few artifacts. Mostly only some that originate from beam hardening due to the use of unfiltered X-radiation from an X-tube. On the other hand, images taken from batch H1, shown in figures 12(b) and 12(e), contain all of the three mentioned above and display a lot more artifacts. Nevertheless, the phases in all of the images were well defined, which was the main focus of this study.

As can be understood from the section, 3.1 the phases in the images are well defined and allow the identification of the phases. Especially with samples without the three main artifact-introducing components mentioned above, in images from these batches, the only phase separated from NC and pores is  $\text{KC}_4\text{H}_5\text{O}_6$  which has about 1.5 times the pixel value of NC around it. This does introduce barely noticeable streak and dark band artifacts around the  $\text{KC}_4\text{H}_5\text{O}_6$  particle, but the effect is so

minor that it does not affect analysis, and no one can notice them without looking for the artifacts. Figure 13(a) however, indicates that a higher concentration of  $\text{KC}_4\text{H}_5\text{O}_6$  particles would affect the images more clearly. Cupping artifacts are also relevant in the images of more simple grains but affect mainly the surrounding area around the grain by darkening it. Cupping artifacts are seen to some extent in all of the images, regardless of the material components, making them not only found in images of simpler recipe propellant grains.

More attenuating particles like  $\text{K}_2\text{SO}_4$  introduce more beam hardening into the images and can also introduce some photon starvation and therefore star artifacts. This was the main reason why an acceleration voltage of 60 kV was chosen and not 40 kV which would have been more optimal for measurements done on particles made from NC. Higher voltage reduced the star artifacts from the  $\text{K}_2\text{SO}_4$  particles while still maintaining good contrast between pores and NC. I also deemed pre-filtering of the X-radiation to not be beneficial due to the loss of contrast in NC and only minor benefits in artifact reduction.

I previously mentioned how  $\text{K}_2\text{SO}_4$  had a pixel value of about 50 000. This is almost twice the amount of average NC value in the image, at around 21 000. This difference is enough to introduce clear streak and dark band artifacts, like seen in figures 12(a), 12(b) and 12(e) and especially in the reference sample 13(d). The size of the particle also affects the magnitude of the artifact, with a larger particle introducing a higher magnitude of artifact into the images. Stronger artifacts can increase or reduce the size of the particle itself and others around it, or hide some phases completely. The effect on the identification process was notable, as demonstrated by the unsuccessful reference sample for  $\text{K}_2\text{SO}_4$  sulfate, which affected the code analysis by introducing new pores and dense particles that were not there.

Similarly to  $\text{K}_2\text{SO}_4$ , metals Sn and Bi introduced star artifacts and beam hardening, although with a higher effect. X-rays are attenuated almost totally by the metals, causing heavy artifacts, making some cross-section images full of streaks and dark bands from star artifacts. Both of the metals have such a high attenuation coefficient that they can not be identified from each other in the images and can easily hide some phases behind the "shine" of the star artifacts. Luckily, most of the particles are small and do not cause thick strikes, making images usable in code analysis. Although thin, the strikes can still cut near-by pores and particles in half, making them seem like two separate ones instead of one. More porous grains suffer the most from this because metal particles have to be near the pores because the walls between the pores are so thin. The size of the metal particle is also exaggerated by the "shine" of the star artifact in all of the grains, which is also true for some bigger  $\text{K}_2\text{SO}_4$  particles.

Although the unidentified, more malleable looking phase had partially the same pixel value as the metals, it did not cause as severe artifacts as did the metal. Somehow the shine is locally worse in samples with  $\text{K}_2\text{SO}_4$  particles, which is unexpected. Higher pixel values correlate with a higher attenuation coefficient, which in turn usually means more beam hardening and possible photon starvation. It is safe to assume that the unidentified material is not as attenuating as the two metals found in N and HE-types, but I would not say for certain that it is more attenuating than  $\text{K}_2\text{SO}_4$  particles. Because the unidentified phases do not cause severe artifacts, the images are very well defined and are as good as samples, with only  $\text{KC}_4\text{H}_5\text{O}_6$  as the most attenuating component.

Grains from batches N6-N8 have some blurriness at the edges, which is shown in figure 12(d). The asymmetric geometry of the cross-sections in the grains made it so that parts of the grains were outside of the FOV in some projections, causing incomplete projection artifacts. Images were distorted at the tips of the T-shaped cross-section, making it hard to identify where the grain stops and the background starts. Artifacts were mostly located at either the top or bottom end of the grain. This allowed me to cut distorted areas out before analysis, so I did not deem it necessary to measure the grains with  $10\times$  magnification instead of  $20\times$ .

### 3.3 Image analysis with Python script

The mean values of all the measured parameters, porosity, pore diameter, wall diameter, and dense particle diameter are presented in table 3. The values represented in the table are the means of the two propellant grains from each batch with the respective variation between the two grains (variation is the difference between the two values of individual grains divided by the mean value). In most cases, the script calculated the proper mean pore sizes, but for some with a bigger FOV (measurements done with  $10\times$  magnification) or a smaller middle hole (grain-specific), the pore size was affected by the middle hole. Because the hole size did not affect all of the samples, I measured the hole diameter for all of the samples, and if I saw the hole diameter in the distribution of pore sizes, I removed it and recalculated the mean pore value. This calculation was done for both grains in batches N5, H7, H8 and T1.

High variations, which could already be noticed from the qualitative analysis, are confirmed by the large variations between most of the grains. On average, variation was 19 % at porosity, 31 % at pore size, 26 % at wall diameter, and 29 % at dense particle size. This makes porosity the most stable measured variable. The highest variation in this was found in N5, but this is due to the low porosity of the grains; a single bigger pore in either of the two grains could cause the difference. The smallest variation between the two grains was in the more porous batches, N6-N8.

Table 3: Averages of the two grains measured from each batch acquired with script analysis. Variation is the the difference between the two grains and divided by the mean value.

Sample	Porosity	Porosity variation (%)	Pore size ( $\mu\text{m}$ )	Pore size variation (%)	Wall diameter ( $\mu\text{m}$ )	Wall diameter variation (%)	Dense particle size ( $\mu\text{m}$ )	Dense particle size variation (%)
N1	0.10	3	20	12	44	5	26	56
N2	0.12	5	21	39	33	24	16	35
N3	0.06	19	28	52	49	30	23	5
N4	0.07	38	28	7	41	4	30	4
N5	0.05	42	24	88	59	36	23	10
N6	0.50	1	22	7	8	20	8	29
N7	0.50	0	21	3	8	8	11	19
N8	0.30	2	25	11	15	19	15	21
H1	0.07	2	34	57	46	42	19	11
H2	0.10	22	30	21	31	20	19	25
H3	0.04	32	59	6	83	4	41	66
H4	0.12	20	37	21	28	28	27	71
H5	0.17	33	25	46	16	75	29	70
H6	0.19	38	27	9	17	48	18	12
H7	0.09	15	15	19	26	10	16	42
H8	0.11	12	13	34	24	19	15	13
T1	0.08	47	17	27	31	14	13	16
T2	0.10	23	20	28	43	13	15	11

This is most likely due to the high porosity, which limits the effect of individual pores on the average pore size and wall diameter. In N7 and N8, the dense particle size has higher average variation due to all of the dense particles being metals seen as star artifacts. Like previously mentioned, star artifacts make them randomly look bigger, which is most likely the cause for the comparatively larger variation (compared to other variations in batches N7 and N8).

Above, I had a correlation showing that higher porosity meant less variation in measured variables between the two grains. The porosity of the propellant is controlled by the amount of  $\text{KNO}_3$  used during production. I found that it has the highest and most notable relationship to the measured variables. Figure 14 presents the variables as a function of  $\text{KNO}_3$  content used during the production. The horizontal axis shows how many kilograms of  $\text{KNO}_3$  is used per 150 kg of NC mass during the production. Porosity rises with the  $\text{KNO}_3$  quantity, but pore diameter, wall diameter, and dense particle size get smaller. These can be explained by the role of  $\text{KNO}_3$  in the production process: It is introduced into the NC mass at the gelatination step and is then moved along the production steps inside the produced grains as small grain-like particles of random size. As highly water-soluble material,  $\text{KNO}_3$  is removed during water treatment, leaving empty spaces inside the propellant grain that are later filled with air during drying.



The correlation with porosity is simple, more  $\text{KNO}_3$  particles containing pre-water treatment grains gain more pores during the process than ones with less  $\text{KNO}_3$  particles inside of them, thus having a larger porosity. This also means that there is less space between the pores, or, in other words, less volume between the pores, and thus a lower wall diameter.

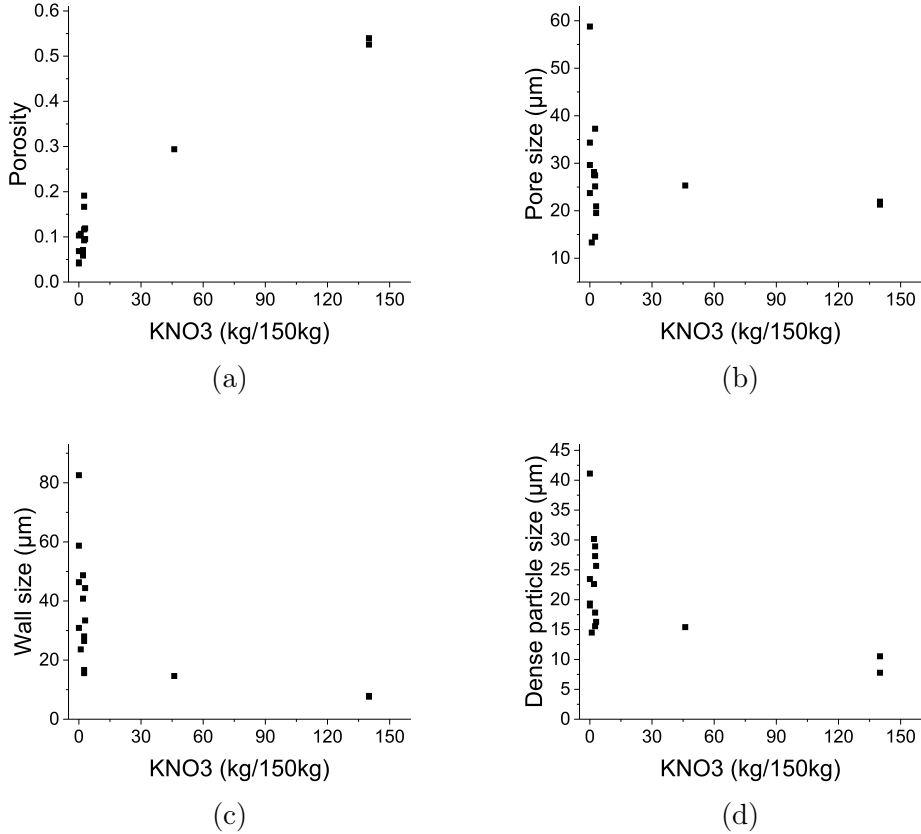


Figure 14: *Porosity, pore size, wall diameter, and dense particle size plotted as a function of  $\text{KNO}_3$  salt amount used during the production.*

To explain the effect  $\text{KNO}_3$  content has to pore sizes, one needs to consider that  $\text{KNO}_3$  grains have random diameter at some range  $[d, D]$ , where  $0 < d < D$  and average particle size is  $D_a = (d + D)/2$ . When  $\text{KNO}_3$  amount is small, the  $\text{KNO}_3$  particles in an individual grain have a bigger chance to differ from  $D_a$  than when there are more of them. This can lead to a larger or smaller average pore size on average, thus the results. It is also possible that the pores shrink more in porous propellant grains. There is not enough NC mass between the pores to hold the original shape of the  $\text{KNO}_3$  grain after it has dissolved, therefore lowering the pore size. This would also effect the geometry of the grain which was not detected in

this study. However, I would still assume that the pore size would be more stable with a larger sample size than two per batch and lose most of the effect seen from  $\text{KNO}_3$  content in this study.

When considering the dense particles, it is good to remember that when analyzing with the script, I deemed all of the particles with higher attenuation than NC as dense particles, in other words  $\text{KC}_4\text{H}_5\text{O}_6$ ,  $\text{K}_2\text{SO}_4$ , Sn, Bi and unidentified materials in T1 and T2. Like pore size, the dense particle size had no relation with  $\text{KNO}_3$  content. The two batches with the most  $\text{KNO}_3$  used in them are N6 and N7 which do not have  $\text{KC}_4\text{H}_5\text{O}_6$  nor  $\text{K}_2\text{SO}_4$  in them, meaning that all of the dense particles in them are the metals Sn and Bi. Metal particles are small compared to  $\text{KC}_4\text{H}_5\text{O}_6$  and  $\text{K}_2\text{SO}_4$  making the detected dense particle size smaller in N6 and N7. The introduction of  $\text{KC}_4\text{H}_5\text{O}_6$  and  $\text{K}_2\text{SO}_4$  into N6 and N7 batches would definitely increase the average size of dense particles. However, it is notable that on average batch N8, seen in the middle of the figures at 14, has a slightly smaller dense particle size than batches with lower usage of  $\text{KNO}_3$ , average of batch N8 being  $15\ \mu\text{m}$  and less  $\text{KNO}_3$  quantity batches being  $22\ \mu\text{m}$ . This could be due to the longer water treatment time required with higher  $\text{KNO}_3$  quantities effecting  $\text{KC}_4\text{H}_5\text{O}_6$  particles sizes (N8 does not have  $\text{K}_2\text{SO}_4$ ) by dissolving it, or that some of the  $\text{KC}_4\text{H}_5\text{O}_6$  splits during the treatment due to the loss of support. For the latter, consider that  $\text{KNO}_3$  grain can be next to  $\text{KC}_4\text{H}_5\text{O}_6$  grain and then dissolve, lowering the support felt by the  $\text{KC}_4\text{H}_5\text{O}_6$  grain. Partial dissolving of  $\text{KC}_4\text{H}_5\text{O}_6$  is considerable unlikely due to its low solubility in water  $0.62\ \text{g}/100\text{ml}$  [82].

## 4 Discussion

X-ray tomography suits well for propellant analysis; images are well defined, and different phases are distinguishable from each other with an X-ray tube source and an acceleration voltage of 60 kV. The large variation of attenuation coefficient inside the propellant grains and asymmetric geometry of some grains, introducing artifacts like beam hardening, photon starvation, and incomplete projection artifacts into the final images. A notable qualitative finding was that the two grains measured from each batch could have highly different inner structures. From the images, I was able to identify the main components in the different phases by using knowledge of the propellant recipe, the process of elimination, and reference images. Main components identified are nitrocellulose mass (NC), potassium bitartrate ( $\text{KC}_4\text{H}_5\text{O}_6$ ), potassium sulfate ( $\text{K}_2\text{SO}_4$ ), surface finishing compound (SFC), and some metals known to be Tin (Sn) and Bismuth (Bi). Unfortunately, a lack of information on batches T1 and T2 prevented the identification of one clearly different phase in the two batches. Results and the unidentified phase are presented in figure 15. The two metals could not be identified from each other due to their similar X-ray attenuation and both introducing star artifacts into the images.

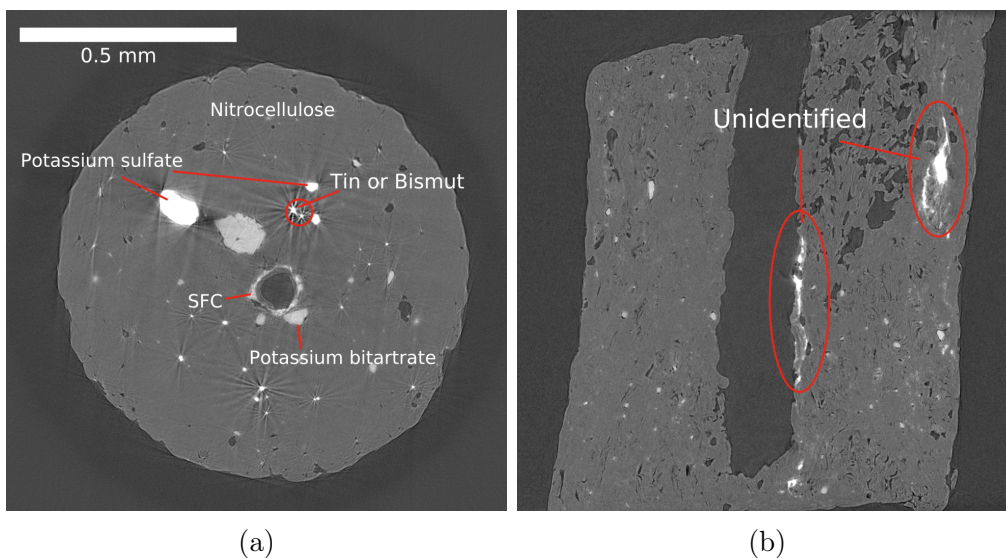


Figure 15: *Phases identified and one unidentified phase inside propellant grains in this study. Both images have the same scale bar seen in a).*

The scripts used to analyze the images were found useful. Qualitatively detected high variation between the two grains from each batch was confirmed via the measured variables: porosity, pore size, thickness of NC mass between the pores (wall size), and size of particles with higher attenuation than NC ( $\text{KC}_4\text{H}_5\text{O}_6$ ,  $\text{K}_2\text{SO}_4$

and the two metals). The mean values of the results can be seen in table 3. The amount of potassium nitrate ( $\text{KNO}_3$ ) used at the production of propellant batch was found to affect the measured variables in the following ways: A higher  $\text{KNO}_3$  quantity means higher porosity and a lower distance between pores (lower wall size). Pores and highly attenuating particles also got smaller when  $\text{KNO}_3$  quantity was increased, but these results are most likely due to a lack of sample size and a lack of some components in batches with higher  $\text{KNO}_3$  contents. My hypothesis is that pore size should be constant on average, unrelated to the  $\text{KNO}_3$  quantity used during production, and that it could be detected with a larger sample size.

Problems in this study originate from the mentioned small sample size, artifacts, inadequate information about batches T1 and T2, and middle hole inclusion in the script analysis. The latest one was just an inconvenience, and I was able to correct most of the middle hole-affected data by manually removing it afterwards. Other possibility would have been to remove the middle hole from the analysis via image processing. Due to the small sample size, all results gathered via Python script analysis are not statistically significant. Only two grains per batch lead to high variation, which excludes batch specific examination of propellant. Two significantly different batches can be compared, but two batches with similar main components cannot.. For example, I was given one bad batch to compare it to the right one, but I could not find any significant difference between the two batches. With a larger sample size, this could be possible, but it should be much larger, which would take hundreds of hours of measurement time with the used equipment and parameters, the Xradia MicroXCT-400. It would take a long time to gather sufficient data. With a synchrotron source the measurements could be made quicker.

The relation between  $\text{KNO}_3$  content and pore size above can be explained by just randomly picking grains with larger pores and not by the amount of  $\text{KNO}_3$  used in production, which could be evened out with a larger sample size. It is also notable that all of the selected grains were vertically standing, excluding all lopsided grains, giving a sample of grains that does not represent all of the grains in a batch. In the future, the rod on which the grain is glued could be made to have a slope in its top end. With a slope of suitable angle, the propellant grain could be parallel with the turning axis at the measurement device, thus not turning out of the FOV at some projection images.

Artifacts were unfortunate features in the images and introduced errors, especially in analysis. Less significant artifacts like beam hardening did not affect the main propellant grain images and analysis in any meaningful way, and most of the cone beam artifacts could be cropped away before analysis. Star artifacts, on the other hand, were more problematic. Previously, I mentioned how some streaks from star

artifacts can cut a pore in half or induce pores and dense particles at locations where there are none. These were found to be especially problematic in porous samples N6–N8, but the most problematic were star artifacts located near the edges of the sample. The shine of the artifacts reached outside of the grain, and the code thought that the grain was larger than it is. Thresholded images  $I$  had therefore something outside of the grain, which was then magnified into mask images  $M$ ; both are demonstrated in figure 16.  $M$  represents the total volume of the grain at a given cross-section (mass and pores included), and when its edges are broader than in image  $I$  all that volume is thought to be pores by the script. This leads to higher porosity and affects the pore size. Similar expansion of  $M$  is found when the grain is near the edges of the image, as demonstrated in figure 16(d), where the lower part of the grain is fused with the edges of the image (note that the image is not from the same cross-section as the others in figure 16). This happens due to specific boundary conditions used in the image analysis routines. Both of these problems could be corrected by different design of the analysis pipeline.

Artifacts were the main reason why one of the reference samples,  $\text{K}_2\text{SO}_4$ , was unsuccessful. The powder of  $\text{K}_2\text{SO}_4$  hardened the beam so much that the images became blurry and could not be used as a reliable reference. Artifacts seen in the images of the reference sample are worse than in propellant grain images containing  $\text{K}_2\text{SO}_4$  which leads me to think that the problem originates from the configuration of the reference sample. Powder surrounding propellant grain enhances all forms of beam hardening artifacts, cupping and streaks, and dark band artifacts. The beam gets harder when it first penetrates reference powder and gets harder again when it exits propellant on the other side, doubling the effect. This effect is also demonstrated by the reference sample for  $\text{KC}_4\text{H}_5\text{O}_6$ , which did not introduce strong beam hardening artifacts in propellant grain images but had them in the reference image.

Higher acceleration voltage and pre-filtering of the X-radiation would help reduce the artifacts by increasing the detected intensity. However, due to the low attenuation of NC mass, I found that if voltage was raised or X-radiation was filtered, it lowered the contrast between NC mass and air (and therefore pores), making analysis via script more inaccurate. I also tried to lower the acceleration voltage and filter the X-radiation, but it did not provide any improvements to the images. On the other hand, a couple of measurements done with higher voltage would have made it possible to differentiate the two metals from each other and would have been better suited for reference samples. Naturally, if reference samples were to be measured with new parameters, a propellant grain should also be included. In the future, I would use algorithms to reduce the artifacts to gain better data. Mainly, I would use algorithms to reduce star artifacts caused by the two metals.

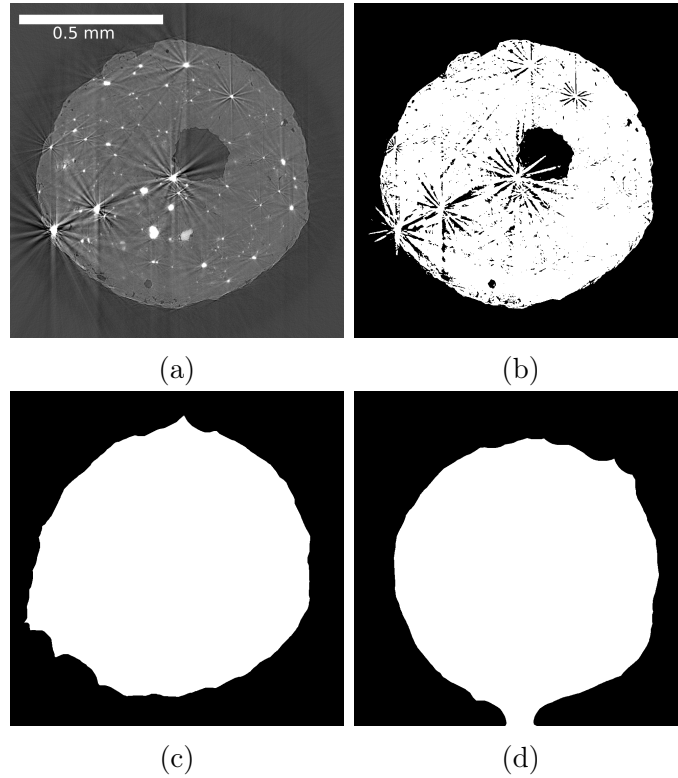


Figure 16: *Demonstration of how star artifacts and grain location relative to the borders of images affect the threshold image and mask made from the CT images. a-c) are from the same cross-section of a grain from H2 batch, b) is the thresholded and c) the mask image. d) is from the same grain but from a cross-section where grain edge is closer to the image border. c) and d) show how the grain borders can be misrepresented during at the script analysis. Note that scale bar in image a) is the same for all the images.*

Algorithms like these are mainly used in the medical field, where the patient can have metals inside their body like dental implants [66, 83, 84].

The study's focus on dense particles was a little too broad. I defined them as everything inside the propellant grain with a higher attenuation coefficient than NC mass, which combines  $\text{KC}_4\text{H}_5\text{O}_6$ ,  $\text{K}_2\text{SO}_4$  and metals as the same phase according to the script. To gain more reliable and comparable data between the different batches, the approach should be more material-specific. In the future, new configurations for the reference samples should have the powder in smaller quantities inside the NC mass or something with a similar attenuation coefficient. Also energy sensitive X-CT could be able to identify the Sn- and Bi-particles from each others.

In conclusion, X-CT provides valuable information about the inner structure of a single propellant grain with high contrast and resolution, allowing comparison between different batches and interior particle identification. This study provides evidence that  $\mu$ X-CT can be used to identify multiple different components by comparing different samples with different compositions. In the future, the methods presented could be used to analyze similar chemical samples to gain knowledge of their physical structure and how the different components are preserved inside the samples. Also, with better access to artifact-limiting algorithms, one could gain even more precise information about the inner structure of propellant grains.

## References

- [1] J. Needham and T. Tsuen-Hsuin. *Science and Civilisation in China, Chemistry And Chemical Technology, Part 7, Military Technology, The Gunpowder Epic*, volume 5. 1986.
- [2] E. Paananen. *Messinkihylsyisten keskisytytyspatruunoiden jälleenlataus*. Bookwell Oy, 5 edition, 2011.
- [3] Group SNPE. *An introduction to energetic materials*.
- [4] E. B. F. Galante F. D. Botelho and A. J. B. Mendes. Characteristics and manufacture of spherical smokeless powders, 2015.
- [5] A. S. Tremsin, J. B. McPhate, J. V. Vallerga, O. H.W. Siegmund, W. B. Feller, E. Lehmann, L. G. Butler, and M. Dawson. High-resolution neutron microtomography with noiseless neutron counting detector. volume 652, 2011.
- [6] R. F. Mould. The early history of X-ray diagnosis with emphasis on the contributions of physics 1895-1915. *Physics in Medicine and Biology*, 40:1741–1787, 11 1995.
- [7] G. N. Hounsfield. Computerized transverse axial scanning (tomography): Part 1. description of system. *The British Journal of Radiology*, 46:1016–1022, 12 1973.
- [8] J. Gawler, M. D. Sanders, J. W. Bull, G. du Boulay, and J. Marshall. Computer assisted tomography in orbital disease. *British Journal of Ophthalmology*, 58:571–587, 6 1974.
- [9] C. Richmond. Sir Godfrey Hounsfield. *BMJ*, 329:687.1, 9 2004.
- [10] V. Cnudde and M.N. Boone. High-resolution X-ray computed tomography in geosciences: A review of the current technology and applications. *Earth-Science Reviews*, 123:1–17, 8 2013.
- [11] M. Onoe, J. W. Tsao, H. Yamada, H. Nakamura, J. Kogure, H. Kawamura, and M. Yoshimatsu. Computed tomography for measuring annual rings of a live tree. *Proceedings of the IEEE*, 71:907–908, 1983.
- [12] G. C. Conroy and Michael W. Vannier. Dental development of the taung skull from computerized tomography. *Nature*, 329:625–627, 10 1987.
- [13] A. M. Petrovic, J. E. Siebert, and P. E. Rieke. Soil bulk density analysis in three dimensions by computed tomographic scanning. *Soil Science Society of America Journal*, 46:445–450, 5 1982.



- [14] X. Boespflug, B.F.N. Long, and S. Occhietti. CAT-scan in marine stratigraphy: a quantitative approach. *Marine Geology*, 122:281–301, 2 1995.
- [15] H. J. Vinegar and S. L. Wellington. Tomographic imaging of three-phase flow experiments. *Review of Scientific Instruments*, 58:96–107, 1 1987.
- [16] J. Yoon, H. Kim, S. H. Sim, and S. Pyo. Characterization of porous cementitious materials using microscopic image processing and X-ray CT analysis. *Materials*, 13, 2020.
- [17] G. Kerckhofs, J. Schrooten, T. Van Cleynenbreugel, S. V. Lomov, and M. Wevers. Validation of X-ray microfocus computed tomography as an imaging tool for porous structures. *Review of Scientific Instruments*, 79:013711, 1 2008.
- [18] Maire and Eric. X-ray tomography applied to the characterization of highly porous materials. *Annual Review of Materials Research*, 42(1):163–178, 2012.
- [19] Vihtavuori Tech Team. Tech blog: Powder grain shapes. <https://www.vihtavuori.com/tech-blog-powder-grain-shapes/>.
- [20] D. M. Northrop. Gunshot residue analysis by micellar electrokinetic capillary electrophoresis: Assessment for application to casework. part ii. *Journal of Forensic Sciences*, 46, 2001.
- [21] K. Balser, H. Lutz, T. Eicher, M. Wandel, H-J. Astheimer, H. Steinmeier, and J. M. Allen. *Ullmann's Encyclopedia of Industrial Chemistry*. Wiley, 3 2003.
- [22] M. A. Fernández de la Ossa, M. López-López, M. Torre, and C. García-Ruiz. Analytical techniques in the study of highly-nitrated nitrocellulose. *TrAC Trends in Analytical Chemistry*, 30:1740–1755, 12 2011.
- [23] V. C. Marshall. Nitrocelluloses, the materials and their applications in propellants, explosives and other industries. *Journal of Hazardous Materials*, 30, 1992.
- [24] R. M. Heramb and B. R. McCord. The manufacture of smokeless powders and their forensic analysis: A brief review. *Forensic Science Communications*, 4, 2002.
- [25] L. Dauerman and Y. A. Tajima. Thermal decomposition and combustion of nitrocellulose. *AIAA Journal*, 6:1468–1473, 8 1968.

- [26] Y. He, Y. He, J. Liu, P. Li, M. Chen, R. Wei, and J. Wang. Experimental study on the thermal decomposition and combustion characteristics of nitrocellulose with different alcohol humectants. *Journal of Hazardous Materials*, 340, 2017.
- [27] R. Wei, S. Huang, Z. Wang, X. Wang, C. Ding, R. Yuen, and J. Wang. Thermal behavior of nitrocellulose with different aging periods. *Journal of Thermal Analysis and Calorimetry*, 136, 2019.
- [28] Y. Zhao, B. Jin, R. Peng, and L. Ding. Interaction of nitrocellulose with pentacycloxyphenyl fullerene derivatives: autocatalytic inhibition in thermal decomposition of nitrocellulose. *Cellulose*, 27, 2020.
- [29] Nammo Lapua Oy. *Reloading manual*. Gummerus Kirjapaino Oy, 2006.
- [30] G. Stark. X-ray, radiation beam, 5 2023.
- [31] E. Merzbacher and H. W. Lewis. X-ray production by heavy charged particles, 1958.
- [32] P. J. Withers, C. Bouman, S. Carmignato, V. Cnudde, D. Grimaldi, C. K. Hagen, E. Maire, M. Manley, A. D. Plessis, and S. R. Stock. X-ray computed tomography. *Nature Reviews Methods Primers*, 1:18, 2 2021.
- [33] A. Burvall, U. Lundström, R. A. C. Takman, D. H. Larsson, and H. M. Hertz. Phase retrieval in X-ray phase-contrast imaging suitable for tomography. *Optics Express*, 19, 2011.
- [34] B. J. Heismann, J. Leppert, and K. Stierstorfer. Density and atomic number measurements with spectral X-ray attenuation method. *Journal of Applied Physics*, 94:2073–2079, 8 2003.
- [35] B.L. Henke, E.M. Gullikson, and J.C. Davis. X-ray interactions: Photoabsorption, scattering, transmission, and reflection at  $E = 50\text{--}30,000$  eV,  $Z = 1\text{--}92$ . *Atomic Data and Nuclear Data Tables*, 54:181–342, 7 1993.
- [36] R. A. Rutherford, B. R. Pullan, and I. Isherwood. X-ray energies for effective atomic number determination. *Neuroradiology*, 11:23–28, 1976.
- [37] L. Grodzins. Optimum energies for X-ray transmission tomography of small samples. *Nuclear Instruments and Methods in Physics Research*, 206:541–545, 3 1983.
- [38] T. Jensen, T. Aljundi, J. N. Gray, and R. Wallingford. A model of X-ray film response, 1996.

- [39] J. Chen, R. Mao, L. Zhang, and R. Y. Zhu. Large size LSO and LYSO crystals for future high energy physics experiments. *IEEE Transactions on Nuclear Science*, 54, 2007.
- [40] Claus Grupen and Irène Buvat. *Handbook of Particle Detection and Imaging*. Springer Berlin Heidelberg, 2012.
- [41] C. Amsler, M. Doser, M. Antonelli, D.M. Asner, K.S. Babu, H. Baer, H.R. Band, R.M. Barnett, E. Bergren, J. Beringer, G. Bernardi, W. Bertl, H. Bichsel, O. Biebel, P. Bloch, E. Blucher, S. Blusk, R.N. Cahn, M. Carena, C. Caso, A. Ceccucci, D. Chakraborty, M.-C. Chen, R.S. Chivukula, G. Cowan, O. Dahl, G. D’Ambrosio, T. Damour, A. de Gouvêa, T. DeGrand, B. Dobrescu, M. Drees, D.A. Edwards, S. Eidelman, V.D. Elvira, J. Erler, V.V. Ezhela, J.L. Feng, W. Fetscher, B.D. Fields, B. Foster, T.K. Gaisser, L. Garren, H.-J. Gerber, G. Gerbier, T. Gherghetta, G.F. Giudice, M. Goodman, C. Grab, A.V. Gritsan, J.-F. Grivaz, D.E. Groom, M. Grünewald, A. Gurtu, T. Gutsche, H.E. Haber, K. Hagiwara, C. Hagmann, K.G. Hayes, J.J. Hernández-Rey, K. Hikasa, I. Hinchliffe, A. Höcker, J. Huston, P. Igo-Kemenes, J.D. Jackson, K.F. Johnson, T. Junk, D. Karlen, B. Kayser, D. Kirkby, S.R. Klein, I.G. Knowles, C. Kolda, R.V. Kowalewski, P. Kreitz, B. Krusche, Yu.V. Kuyanov, Y. Kwon, O. Lahav, P. Langacker, A. Liddle, Z. Ligeti, C.-J. Lin, T.M. Liss, L. Littenberg, J.C. Liu, K.S. Lugovsky, S.B. Lugovsky, H. Mahlke, M.L. Mangano, T. Mannel, A.V. Manohar, W.J. Marciano, A.D. Martin, A. Masoni, D. Milstead, R. Miquel, K. Mönig, H. Murayama, K. Nakamura, M. Narain, P. Nason, S. Navas, P. Nevski, Y. Nir, K.A. Olive, L. Pape, C. Patrignani, J.A. Peacock, A. Piepke, G. Punzi, A. Quadt, S. Raby, G. Raffelt, B.N. Ratcliff, B. Renk, P. Richardson, S. Roesler, S. Rolli, A. Romaniouk, L.J. Rosenberg, J.L. Rosner, C.T. Sachrajda, Y. Sakai, S. Sarkar, F. Sauli, O. Schneider, D. Scott, W.G. Seligman, M.H. Shaevitz, T. Sjöstrand, J.G. Smith, G.F. Smoot, S. Spanier, H. Spieler, A. Stahl, T. Stanev, S.L. Stone, T. Sumiyoshi, M. Tanabashi, J. Terning, M. Titov, N.P. Tkachenko, N.A. Törnqvist, D. Tovey, G.H. Trilling, T.G. Trippe, G. Valencia, K. van Bibber, M.G. Vincter, P. Vogel, D.R. Ward, T. Watari, B.R. Webber, G. Weiglein, J.D. Wells, M. Whalley, A. Wheeler, C.G. Wohl, L. Wolfenstein, J. Womersley, C.L. Woody, R.L. Workman, A. Yamamoto, W.-M. Yao, O.V. Zenin, J. Zhang, R.-Y. Zhu, P.A. Zyla, G. Harper, V.S. Lugovsky, and P. Schaffner. Review of particle physics. *Physics Letters B*, 667(1):1–6, 2008.
- [42] A. M. Cormack. Reconstruction of densities from their projections, with applications in radiological physics. *Physics in Medicine and Biology*, 18, 1973.

- [43] R. Schofield, L. King, U. Tayal, I. Castellano, J. Stirrup, F. Pontana, J. Earls, and E. Nicol. Image reconstruction: Part 1 – understanding filtered back projection and noise and image acquisition. *Journal of Cardiovascular Computed Tomography*, 14:219–225, 5 2020.
- [44] E. Maire and P. J. Withers. Quantitative X-ray tomography. *International Materials Reviews*, 59:1–43, 1 2014.
- [45] S. W. Wilkins, T. E. Gureyev, D. Gao, A. Pogany, and A. W. Stevenson. Phase-contrast imaging using polychromatic hard X-rays rid b-3041-2011 rid a-9209-2011. *Nature*, 384, 1996.
- [46] Y.S. Krivonosov, V. E. Asadchikov, and A. V. Buzmakov. Phase-contrast imaging in a polychromatic X-ray beam at a laboratory source. *Crystallography Reports*, 65:503–507, 7 2020.
- [47] M. Wu, A. Keil, D. Constantin, J. Star-Lack, L. Zhu, and R. Fahrig. Metal artifact correction for X-ray computed tomography using kv and selective mv imaging. *Medical Physics*, 41:121910, 11 2014.
- [48] M. Krenkel, M Töpperwien, C Dullin, F Alves, and T. Salditt. Propagation-based phase-contrast tomography for high-resolution lung imaging with laboratory sources. *AIP Advances*, 6:035007, 3 2016.
- [49] D. H. Larsson, W. Vågberg, A. Yaroshenko, A. Ö. Yildirim, and H. M. Hertz. High-resolution short-exposure small-animal laboratory X-ray phase-contrast tomography. *Scientific Reports*, 6, 2016.
- [50] A. Bravin, P Coan, and P. Suortti. X-ray phase-contrast imaging: From pre-clinical applications towards clinics, 2013.
- [51] P. Toft. The radon transform, theory and implementation, 1996.
- [52] J. Laitinen. Kappaleen sisäisen tarkastelutilavuuden rekonstruointi röntgentomografiassa, 2018.
- [53] R. Radke. Lecture 18: Reconstruction from parallel projections and the radon transform. <https://www.youtube.com/watch?v=ZgcD4C-4u0Q&t=3416s>, 2015. Intro to Digital Image Processing (ECSE-4540) Lectures, accessed 15.5.2023.
- [54] A. Miettinen. <https://github.com/arttumiettinen/pi2>.
- [55] J. F. Barrett and N. Keat. Artifacts in CT: Recognition and avoidance. *RadioGraphics*, 24:1679–1691, 11 2004.

- [56] S. P. Osipov, S. V. Chakhlov, V. Y. Zhvyrblia, D. A. Sednev, O. S. Osipov, and E. Y. Usachev. The nature of metal artifacts in X-ray computed tomography and their reduction by optimization of tomography systems parameters. *Applied Sciences*, 13:2666, 2 2023.
- [57] M. Diwakar and Manoj Kumar. A review on CT image noise and its denoising. *Biomedical Signal Processing and Control*, 42:73–88, 4 2018.
- [58] A. J. Warren, D. Axford, and R. L. Owen. Direct measurement of X-ray-induced heating of microcrystals. *Journal of Synchrotron Radiation*, 26:991–997, 7 2019.
- [59] M. Eldib, M. Hegazy, Y. Mun, M. Cho, M. Cho, and Soo Lee. A ring artifact correction method: Validation by micro-ct imaging with flat-panel detectors and a 2d photon-counting detector. *Sensors*, 17:269, 1 2017.
- [60] X. Tang, E. A. Krupinski, H. Xie, and A. E. Stillman. On the data acquisition, image reconstruction, cone beam artifacts, and their suppression in axial MDCT and CBCT - a review. *Medical Physics*, 45:761–782, 9 2018.
- [61] K. An, J. Wang, R. Zhou, F. Liu, and W. Wu. Ring-artifacts removal for photon-counting CT. *Optics Express*, 28:25180, 8 2020.
- [62] R. A. Brooks and G. Di Chiro. Beam hardening in X-ray reconstructive tomography. *Physics in Medicine and Biology*, 21, 1976.
- [63] A. J. Duerinckx and A. Macovski. Polychromatic streak artifacts in computed tomography images. *Journal of Computer Assisted Tomography*, 2, 1978.
- [64] P. Sukovic and N.H. Clinthorne. Penalized weighted least-squares image reconstruction for dual energy X-ray transmission tomography. *IEEE Transactions on Medical Imaging*, 19:1075–1081, 2000.
- [65] J. Hsieh. Adaptive streak artifact reduction in computed tomography resulting from excessive X-ray photon noise. *Medical Physics*, 25:2139–2147, 11 1998.
- [66] I. Mori, Y. Machida, M. Osanai, and K. Inuma. Photon starvation artifacts of X-ray CT: their true cause and a solution. *Radiological Physics and Technology*, 6:130–141, 1 2013.
- [67] S. R. Stock. X-ray microtomography of materials. *International Materials Reviews*, 44:141–164, 4 1999.
- [68] Sys — system-specific parameters and functions. <https://docs.python.org/3/library/sys.html#module-sys>, 2023. Accessed 15.6.2023.

- [69] Numpy documentation. <https://numpy.org/doc/stable/>, 2022. Accessed 15.6.2023.
- [70] Matplotlib 3.8.0.dev1331+ge80cd214a8 documentation. <https://matplotlib.org/devdocs/index.html>, 2023. Accessed 15.6.2023.
- [71] Tabulate 0.9.0. <https://pypi.org/project/tabulate/>, 2022. Accessed 15.6.2023.
- [72] Csv — csv file reading and writing. <https://docs.python.org/3/library/csv.html>, 2022. Accessed 15.6.2023.
- [73] Pathlib — object-oriented filesystem paths. <https://docs.python.org/3/library/pathlib.html>, 2022. Accessed 15.6.2023.
- [74] A. Miettinen. pi2 documentation. <https://github.com/arttumiettinen/pi2>, 2020.
- [75] C. Tomasi and R. Manduchi. Bilateral filtering for gray and color images. 1998.
- [76] F. Banterle, M. Corsini, P. Cignoni, and P. Scopigno. A low-memory, straightforward and fast bilateral filter through subsampling in spatial domain. *Computer Graphics Forum*, 31:19–32, 2 2012.
- [77] H. J. A. M. Heijmans. Connected morphological operators for binary images. *Computer Vision and Image Understanding*, 73, 1999.
- [78] T. Hildebrand and P. Rügsegger. A new method for the model-independent assessment of thickness in three-dimensional images. *Journal of Microscopy*, 185:67–75, 1 1997.
- [79] A. Miettinen, E. Borisova, M. Stampanoni, and G. Lovric. Separable distributed local thickness algorithm for efficient morphological characterization of terapixel-scale volume images. *In press*.
- [80] Pubchem compound summary for cid 44263835, cellulose nitrate, Accessed 30 May, 2023.
- [81] Pubchem compound summary for cid 4510, nitroglycerin, Accessed 30 May, 2023.
- [82] Pubchem compound summary for cid 23666342, potassium bitartrate, Accessed 30 May, 2023.

- [83] A. Mouton, N. Megherbi, K. Van Slambrouck, J. Nuyts, and T. P. Breckon. An experimental survey of metal artefact reduction in computed tomography. *Journal of X-Ray Science and Technology*, 21:193–226, 2013.
- [84] M. Kidoh, T. Nakaura, S. Nakamura, S. Tokuyasu, H. Osakabe, K. Harada, and Y. Yamashita. Reduction of dental metallic artefacts in CT: Value of a newly developed algorithm for metal artefact reduction (O-MAR). *Clinical Radiology*, 69:e11–e16, 1 2014.

## A Python script for image analysis in this thesis

```
"""
Created on Wed Jun 29 14:51:41 2022

@author: Lenni Syrjanen and Arttu Miettinen
"""
#import used packages
import sys
sys.path.append('C:/Users/lenni/pi2_v4.3-win-no-openc1')
import numpy as np
from pi2py2 import *
pi = Pi2()
pi.echo(True, True)
import matplotlib.pyplot as plt
from tabulate import tabulate
import timeit
from datetime import datetime
import csv
from pathlib import Path

#DEFINE FUNCTIONS WHICH ARE CALLED LATER AT ONCE TO ANALYSE SAMPLE

#define denoising function.
#This function is not included into the function running all the operations, need to
be ran separate
def denoise(sample_name):
    #Read which you want to analyse, denoises it and saves it as denoise
    img = pi.read(f"{sample_name}")
    res = pi.newlike(img)
    pi.bilateralfilter(img, res, 1.5, 20000)
    pi.writeraw(res, f"{sample_name}_denoised")

#Define functions for defining what we want to see in our analysis
#Define functions which sort pores from the normal mass of the sample. Makes mask at
the same time
def threshold(sample_name, threshold1, thres2, folder, closing, run_type):
    #Read denoised image and thresholds it with threshold1 and saves it as bin
    img = pi.read(f"{sample_name}_denoised")
    pi.threshold(img, threshold1)
    pi.convert(img, ImageDataType.UINT8)
    pi.writeraw(img, f"{folder}/{run_type}/{sample_name}_{threshold1}-{thres2}/{
sample_name}_bin")

    #form mask of the sample: everything beyond powder is 0 and inside 1 and saves as
mask
    pi.closingfilter(img, closing)
    pi.writeraw(img, f"{folder}/{run_type}/{sample_name}_{threshold1}-{thres2}/{
sample_name}_mask")

#Sort only denser parts from normal mass of the sample. Makes mask of the sample
def threshold_dense(sample_name, threshold1, threshold2, closing, folder, run_type):
    #Read the denoised image thresholds it to show all mass in grains as 1 and then
close the pores inside

    #and saves it.
    mask = pi.read(f"{sample_name}_denoised")
```



```

pi.threshold(mask, threshold1)
pi.convert(mask, ImageDataType.UINT8)
pi.closingfilter(mask, closing)
pi.writeraw(mask, f"{folder}/{run_type}/{sample_name}_{threshold1}-{threshold2}/{
    sample_name}_mask")
#Read the denoised image and threshold it so that dense particles have value 1
    and everything else is 0
#subtract mask from the newly made image and save it.
img = pi.read(f"/home/tomouser/tank/work-large/RuutiN/analysis/{sample_name}
    _denoised")

pi.threshold(img, threshold2)
pi.convert(img, ImageDataType.UINT8)
pi.subtract(mask, img)
pi.writeraw(mask, f"{folder}/{run_type}/{sample_name}_{threshold1}-{threshold2}/{
    sample_name}_bin")

#Calculate wall diameter
def wall_diameter(sample_name, folder, thres1, thres2, run_type, tmap_mode):
    #Read bin image and forms a plank image capable to hold bigger values.
    geom = pi.read(f"{folder}/{run_type}/{sample_name}_{thres1}-{thres2}/{sample_name}
        _bin")

    tmap = pi.newimage(ImageDataType.FLOAT32)
    #Convert bin image to be capable to hold higher number values and uses pi.tmap to
        make a thickness map
    # out of it, which holds information about wall thickness. Then saving the
        thickness map.

    pi.convert(geom, ImageDataType.UINT32)
    pi.tmap(geom, tmap, 0, False, tmap_mode)
    pi.writeraw(tmap, f"{folder}/{run_type}/{sample_name}_{thres1}-{thres2}/{
        sample_name}_wall_diameter")

#calculate pore diameters
def pore_diameter(sample_name, folder, thres1, thres2, run_type, tmap_mode):
    #read image with pores or denser parts.
    geom = pi.read(f"{folder}/{run_type}/{sample_name}_{thres1}-{thres2}/{sample_name}
        _bin")

    #Changes the images so that the pores or dense parts have value one and
        everything else 0.
    mask = pi.read(f"{folder}/{run_type}/{sample_name}_{thres1}-{thres2}/{sample_name}
        _mask")

    pi.linmap(mask, 0, 1, 1, 0)
    pi.add(geom, mask)
    pi.threshold(geom, 0)
    pi.linmap(geom, 0, 1, 1, 0)
    #write all images in stack separatively to a folder
    pi.writesequence(geom, f"{folder}/{run_type}/{sample_name}_{thres1}-{thres2}/{
        sample_name}_type_masked")

    tmap = pi.newimage(ImageDataType.FLOAT32)
    #calculate local thickness map of the pores and save it.
    pi.convert(geom, ImageDataType.UINT32)
    pi.tmap(geom, tmap, 0, False, tmap_mode)
    pi.writeraw(tmap, f"{folder}/{run_type}/{sample_name}_{thres1}-{thres2}/{
        sample_name}_pore_diameter")

```

```

#calculate the porosity of the sample
def porosity(sample_name, folder, thres1, thres2, run_type):
    #Read bin and mask images, and forms a new 1x1 image capable of holding higher
    # pixel values and
    #sums bin image with the new image. Sum is number of pixels with value 1 in bin
    # image.
    geom = pi.read(f"{folder}/{run_type}/{sample_name}_{thres1}-{thres2}/{sample_name}
    _bin")
    mask = pi.read(f"{folder}/{run_type}/{sample_name}_{thres1}-{thres2}/{sample_name}
    _mask")

    out = pi.newimage(ImageDataType.UINT64)
    pi.sum(geom, out)
    #define fiber count to be global so it can be called later and the value saved
    # into
    #variable out is saved as fibre_count variable.
    global fibre_count
    fibre_count = out.get_value()
    #calculates the number of mask pixels with value 1 and save it into total_count
    # variable.
    pi.sum(mask, out)
    global total_count
    total_count = out.get_value()
    #define porosity to be global so it can be called later and calculates it
    global porosity
    porosity = (total_count - fibre_count) / (total_count)

#define function to calculate normalized distribution of pore or wall diameter,
# depending on the input "diameter_type"
def calc_distr(sample_name, diameter_type, pixel_size, folder, thres1, thres2,
    run_type):

    img = pi.read(f"{folder}/{run_type}/{sample_name}_{thres1}-{thres2}/{sample_name}
    _{diameter_type}")

    # Calculate histogram
    hist_min = 0          # Start of the first bin
    hist_max = 200        # End of the last bin
    bin_count = 100       # Count of bins
    hist = pi.newimage(ImageDataType.FLOAT32)
    bins = pi.newimage(ImageDataType.FLOAT32)
    pi.hist(img, hist, bins, hist_min, hist_max, bin_count)

    # Get histogram data as NumPy array
    data = hist.get_data()
    bin_starts = bins.get_data()

    # Most of the background pixels are in the first bin.
    # We set it to zero so that the output data becomes nicely scaled
    # automatically.
    data[0] = 0

    # Convert bin starts to bin centers
    bin_starts *= pixel_size

```

```

bin_size = bin_starts[1] - bin_starts[0]
bin_centers = bin_starts + bin_size / 2

# Normalize
data /= np.trapz(data, bin_centers)

return bin_centers, data, bin_size

#Define functions to call histogram calculating function and calculate averages for
pore and wall diameters
def diameter_distributions(sample_name, pixel_size, folder, thres1, thres2, run_type)
:
#define both mean values as global for later collections
global mean_p #mean pore diameter
global mean_w #mean wall diameter

#calculate mean pore diameter calling calc_distr with "diameter_type" = "
pore_diameter"
bin_centers_p, hist_p, bin_size = calc_distr(sample_name, "pore_diameter",
pixel_size, folder, thres1, thres2,
run_type)
mean_p = np.average(bin_centers_p, weights=hist_p)
print(f"{run_type} mean pore diameter = {mean_p} \micro m")

#calculate mean wall diameter calling calc_distr with "diameter_type" = "
wall_diameter"
bin_centers_w, hist_w, bin_size = calc_distr(sample_name, "wall_diameter",
pixel_size, folder, thres1, thres2,
run_type)
mean_w = np.average(bin_centers_w, weights=hist_w)
print(f"{run_type} mean wall diameter = {mean_w} \mirco m")

#Save histogram data to csv format for further analysis, if needed.
table = [[sample_name, run_type]]

with open('distribution.csv', 'a', newline='') as csvfile:
writer = csv.writer(csvfile, delimiter=' ',
quotechar='|', quoting=csv.QUOTE_MINIMAL)
writer.writerow(table[0])
writer.writerow('pore/dense data')
writer.writerow(bin_centers_p)
writer.writerow(hist_p)
writer.writerow('wall data')
writer.writerow(bin_centers_w)
writer.writerow(hist_w)

#DEFINE VARIABLES:
# "sample_name" = Name of the sample image.
# Data_type = uint or int 8 to 64 images and float 32 images

# "threshold1 = Define a pixel value for normal mass of the sample. Defined using
some other program like Fiji.
#Used also in directory making.
# Data_type = real number

```

```

# "threshold2" = Define a pixel value for masses with higher pixel values than normal
                  mass of the sample.
                  #Defined using some other program like Fiji. Used also in directory
                  making
#   Data_type = real number

# "pixel_size" = Pixel size of the sample image in micro meters
#   Data_type = real number

# "run_type" = 'true' or 'dense'. Default is 'true'. Depending on do you want to see
                  pores or denser parts.
#               Used also in directory making, separates "true" from "dense" data.
#   Data_type = strings "pore" or "dense"

# "closing" = Diameter determining how big holes are closed when making mask. Default
                  130.
                  #If too big sample can not be properly separated from background
                  during analysis.
                  #If too small bigger pores are lost during analysis
#   Data_type = real number

# "folder" = Folder in which one wants to save formed images and histogram data.
                  Defauly is 'analysis'.
#   Data_type = string

#CALLS ALL THE NEEDED FUNCTIONS TO ANALYSE SAMPLE
def run(sample_name, threshold1, threshold2, pixel_size, run_type = 'true', closing =
        130, folder = 'analysis', tmap_mode =
        False):
    start = timeit.default_timer()          #Start a timer to calculate how long
        running took.
    #get the starting date and time in format (day, month, year   hour:minute:second)
    now = datetime.now()
    dt_string = now.strftime("%d/%m/%Y %H:%M:%S")

    #determine which "run_type" is used
    if run_type == 'true':
        threshold(sample_name, threshold1, threshold2, folder, closing, run_type)

    elif run_type == 'dense':
        threshold_dense(sample_name, threshold1, threshold2, closing, folder,
            run_type)

    else:
        print(f"{run_type} is not right")
        print('options:')
        print('true: only pores are separated from sample')
        print('dense: only dense parts are separated from sample')
        sys.exit()

    pore_diameter(sample_name, folder, threshold1, threshold2, run_type, tmap_mode)
    wall_diameter(sample_name, folder, threshold1, threshold2, run_type, tmap_mode)
    porosity(sample_name, folder, threshold1, threshold2, run_type)

```

```

diameter_distributions(sample_name, pixel_size, folder, threshold1, threshold2,
                        run_type)

#SAVE CALCULATED DATA INTO CSV NAMED "mean_data.csv"
data_table = [[sample_name, f"{run_type}_run"], [dt_string, ], [f"porosity", f"{
porosity}"],
              [f"mean_pore_diameter", f"{mean_p}um"], [f"mean_wall_diameter", f"{mean_w}um"]]

with open('mean_data.csv', 'a', newline='') as csvfile:
    writer = csv.writer(csvfile, delimiter=',',
                        quotechar='|', quoting=csv.QUOTE_MINIMAL)
    writer.writerow(data_table[0])
    writer.writerow(data_table[1])
    writer.writerow(data_table[2])
    writer.writerow(data_table[3])
    writer.writerow(data_table[4])
    writer.writerow(['_-----' * 5])
    writer.writerow([])

#calculate run time and save information about thresholds and closing values so
# when running multiple
# samples at once one can see which have been calculated. Saved to csv file named
# "analysed_samples.csv"

stop = timeit.default_timer()
time_it_took = (stop - start)/60
ran_samples = [[sample_name, run_type, f"time_it_took={time_it_took}_min"], [
threshold1, threshold2, closing]]

with open('analysed_samples.csv', 'a', newline='') as csvfile:
    writer = csv.writer(csvfile, delimiter=',',
                        quotechar='|', quoting=csv.QUOTE_MINIMAL)
    writer.writerow(ran_samples[0])
    writer.writerow(ran_samples[1])
    writer.writerow([])

```